

1  
2  
3  
4  
5  
6  
7  
8  
9  
10  
11  
12  
13  
14  
15  
16  
17  
18  
19  
20  
21  
22

# Slow slip events and megathrust coupling changes reveal the earthquake potential before the 2020 Mw 7.4 Huatulco, Mexico, event

**Authors:** Carlos Villafuerte<sup>1\*</sup>, V. M. Cruz-Atienza<sup>2</sup>, J. Tago<sup>3</sup>, D. Solano-Rojas<sup>3</sup>, R. Garza-Girón<sup>4</sup>, S. I. Franco<sup>2</sup>, L. A. Dominguez<sup>5</sup> and V. Kostoglodov<sup>2</sup>.

November 2020

## Affiliations

<sup>1</sup>Posgrado en Ciencias de la Tierra, Instituto de Geofísica, Universidad Nacional Autónoma de México, Mexico City, Mexico.

<sup>2</sup>Instituto de Geofísica, Universidad Nacional Autónoma de México, Mexico City, Mexico.

<sup>3</sup>Facultad de Ingeniería, Universidad Nacional Autónoma de México, Mexico City, Mexico.

<sup>4</sup>Department of Earth and Planetary Sciences, University of California, Santa Cruz, USA.

<sup>5</sup>Escuela Nacional de Estudios Superiores, Campus Morelia, Universidad Nacional Autónoma de México, Mexico.

\*Correspondence to: villafuerte.cd@gmail.com

## 23 ABSTRACT

24 Stress accumulation on the plate interface of subduction zones is a key parameter that controls the  
25 location, timing and rupture characteristics of earthquakes. The diversity of slip processes occurring  
26 in the megathrust indicates that stress is highly variable in space and time. Based on GPS and  
27 InSAR data, we study in depth the evolution of the interplate slip-rate along the Oaxaca subduction  
28 zone, Mexico, from December 2016 through August 2020, with particular emphasis on the pre-  
29 seismic, coseismic and post-seismic phases associated with the June 23, 2020 Mw 7.4 Huatulco  
30 earthquake to understand how different slip processes contribute to the stress accumulation in the  
31 region. Unlike two time-invariant interplate coupling models previously proposed for the region,  
32 our results show that continuous changes in both the stress-releasing aseismic slip and the coupling  
33 produced a high stress concentration (i.e. Coulomb Failure Stress (CFS) of  $700 \pm 100$  kPa) over  
34 the main asperity of the Huatulco earthquake and a stress shadow zone in the adjacent updip region  
35 (i.e. shallower than 17 km depth with CFS around -500 kPa). These findings may explain both the  
36 downdip rupture propagation (between 17 and 30 km depth) and its impediment to shallower,  
37 tsunamigenic interface regions, respectively. Interplate coupling time variations in the 2020  
38 Huatulco and the nearby 1978 (Mw 7.8) Puerto Escondido rupture zones clearly correlate with the  
39 occurrence of the last three Slow Slip Events (SSEs) in Oaxaca far downdip of both zones,  
40 suggesting that SSEs are systematically accompanied by interplate coupling counterparts in the  
41 seismogenic zone that in turn have their own potentially-seismogenic stress and frictional  
42 implications. In the same period, the interface region of the 1978 event experienced a remarkably  
43 high CFS built-up of 1,000-1,700 kPa, half imparted by the co-seismic and early post-seismic slip  
44 of the neighboring Huatulco rupture, indicating large earthquake potential near Puerto Escondido.  
45 Continuous monitoring of the interplate slip-rate thus provides a better estimation of the stress  
46 accumulation in the seismogenic regions than those given by time-invariant coupling models and

47 improves our understanding of the megathrust mechanics where future earthquakes are likely to  
48 occur.

## 49 **MAIN TEXT**

### 50 **1. Introduction**

51 Large earthquakes occur along subduction zones in regions known as asperities (Lay and Kanamori,  
52 1981), which represent locked areas of the interplate contact where frictional resistance allows  
53 elastic stress to build up during tens to hundreds of years as a consequence of the relative plate  
54 motion. Under the simple concept of Coulomb failure criterion, an earthquake occurs when the  
55 shear stress overcomes the strength of the fault. Both stressing-rate and fault strength are parameters  
56 that vary in time and space during the megathrust earthquake cycle (Moreno et al., 2011). Therefore,  
57 understanding the tectonic processes that cause these variations is essential to assess the seismic  
58 hazard in subduction zones.

59  
60 Inter-seismic coupling maps obtained from geodetic observations have been widely used to identify  
61 heterogenous, highly locked segments of the plate interface where large earthquakes take place  
62 (Chlieh et al., 2008; Loveless and Meade, 2011; Moreno et al., 2010; Perfettini et al., 2010). Most  
63 of these estimations consider a steady-state long term deformation during the inter-seismic periods  
64 that results in a time invariant locking pattern. However, it has been observed that interplate  
65 coupling also varies with time (Heki and Mitsui, 2013; Melnick et al., 2017) and might be caused  
66 by different processes such as pore pressure transients (Cruz-Atienza et al., 2018; Materna et al.,  
67 2019; Warren-Smith et al., 2019) or dynamic stresses from regional earthquakes (Cruz-Atienza et  
68 al., 2020; Delorey et al., 2015; Materna et al., 2019).

69

70 During the inter-seismic period, a broad spectrum of tectonic processes occurs on the plate interface  
71 with distinctive spatiotemporal characteristics that play an important role to accommodate the strain  
72 along the megathrust. Among these processes, short-term and long-term slow slip events (SSEs),  
73 which are aseismic slip transients lasting from days to months, release the strain accumulation in  
74 the deeper and shallower segments of the plate interface (Beroza and Ide, 2011; Saffer and Wallace,  
75 2015). Since their discovery, observations and theoretical models have proposed that SSEs increase  
76 the stress in the adjacent seismogenic zone and may trigger damaging earthquakes (Obara and Kato,  
77 2016; Segall and Bradley, 2012; Uchida et al., 2016; Voss et al., 2018). Moreover, it has been  
78 documented that major interplate earthquakes in different subduction zones are preceded by SSEs,  
79 although the actual mechanisms of their interaction remain under debate.

80

81 In the Mexican subduction zone, the recurrence of Mw 7+ interplate earthquakes is ~30–50 years  
82 (Singh et al., 1981). In the deeper segment of the megathrust (30–50 km depth), long-term SSEs  
83 occur in Oaxaca and Guerrero with recurrence of 1.5 and 3.5 years, respectively (Cotte et al., 2009;  
84 Graham et al., 2016). The last four Mw 7+ interplate events in the Mexican subduction zone were  
85 preceded by SSEs in the downdip adjacent region: The 2014 Mw 7.4 Papanao earthquake in  
86 Guerrero (Radiguet et al., 2016) and three more in Oaxaca, the 2012 Mw. 7.5 Ometepec earthquake  
87 (Graham et al., 2014a), the 2018 Mw 7.2 Pinotepa earthquake (Cruz-Atienza et al., 2020) and, as it  
88 will be shown later, the 2020 Mw 7.4 Huatulco earthquake. These observations suggest that the  
89 prevalent mechanism of the interaction between SSEs and unstable shallower regions in the  
90 Mexican subduction zone is the stress loading from adjacent slow slip processes. Although SSEs  
91 do not always trigger large earthquakes, they do interact periodically with the updip locked regions,  
92 thus contributing with the total stress built-up of the seismogenic zone.

93

94 Three years before the 2020 Huatulco earthquake, a complex sequence of SSEs and devastating  
95 earthquakes took place from June 2017 to July 2019 in central and southern Mexico, including the  
96 Mw 8.2 Tehuantepec and Mw 7.1 Puebla-Morelos earthquakes in 2017, and the Mw 7.2 Pinotepa  
97 earthquake in 2018, describing a cascade of events interacting with each other on a regional scale  
98 via quasi-static and/or dynamic perturbations (Cruz-Atienza et al., 2020). In Oaxaca, the plate  
99 interface slipped (aseismically) almost continuously for the whole two years period with at least  
00 two reactivations, one during the post-seismic relaxation of the Mw 7.2 Pinotepa earthquake, and  
01 the second one with the 2019 Oaxaca SSE.

02

03 Here we thoroughly study the evolution of the interplate slip-rate history in the Oaxaca segment  
04 during this unprecedented sequence including the pre-seismic, coseismic and post-seismic phases  
05 of the 2020 Huatulco earthquake with the aim of understanding how these processes contribute to  
06 the seismic potential in the region. We show that the continuous and simultaneous monitoring of  
07 SSEs and the megathrust coupling provides a better estimation of the stress accumulation on the  
08 locked regions where future large earthquakes are expected to occur.

09

## 10 **2. The 2020 Mw 7.4 Huatulco Earthquake**

11

### 12 **2.1 Coseismic slip inversion**

13

14 On June 23, 2020, a shallow Mw 7.4 interplate thrust earthquake took place below the state of  
15 Oaxaca, Mexico (Fig. 1), with relocated hypocentral coordinates (15.822°, -96.125°, 17.2 km,  
16 determined from seismic records at the station HUAT of the Mexican Servicio Sismológico  
17 Nacional (SSN), which is 7 km south of the epicenter) within the aftershock area of the 1965 Mw  
18 7.5 earthquake, the last interplate rupture in this region (Chael and Stewart, 1982).

19

20 We combined nearfield GPS and Interferometric Synthetic Aperture Radar (InSAR) data to obtain  
21 the coseismic slip distribution by means of ELADIN, a newly developed adjoint inversion method  
22 (Tago et al., 2020) (see Supplementary Materials). For the GPS data we used high rate (1 s) time  
23 series to measure the coseismic static displacement at four stations near the epicenter (Figs. 1c and  
24 S1c-f). The displacement in Huatulco (HUAT station), the closest epicentral site, was carefully and  
25 independently estimated using GPS, tide gauge and strong motion data, yielding very consistent  
26 values of 49 cm uplift and 40 cm seaward displacement (Figs. S1b and S1c). The InSAR line-of-  
27 sight (LOS) displacement map (Figs. 1b and S2) was generated from scenes taken before the  
28 earthquake, on June 19, and two days after the earthquake, on June 25, by the Sentinel satellite of  
29 the European Space Agency on ascending track 107. The InSAR data processing is described in the  
30 Supplementary Materials. For all slip inversions presented in this work we assumed the 3D plate  
31 interface geometry introduced by Cruz-Atienza et al. (2020) and discretized it, for the coseismic  
32 solutions, into subfaults with planar square projections of  $5 \times 5 \text{ km}^2$ .

33

34 To determine the optimal data weights for the joint inversion of GPS and InSAR data we first  
35 inverted each data set independently. Both solution models produced almost a perfect data fit (Figs.  
36 S3a and S3b). The solution using only GPS data describes a very simple and concentrated slip patch  
37 downdip the hypocenter with a maximum value of 4.2 m and a marginally lower than expected  
38 moment magnitude  $M_w$  7.32 with average GPS data error of  $0.2 \pm 0.2 \text{ cm}$  (Fig. S3a). The resulting  
39 model using only InSAR data describes a more heterogeneous slip distribution with maximum  
40 value of 2.5 m and a slightly higher moment magnitude of 7.34 with average InSAR data error of  
41  $0.0 \pm 1.2 \text{ cm}$  (Fig. S3b). Different joint inversion tests led us to optimal data weights (see  
42 Supplementary Materials) producing a final solution that satisfactorily explains both sets of

43 observations with average GPS and InSAR data errors of  $1.2 \pm 1.0$  cm and  $0.2 \pm 2.1$  cm, respectively  
44 (Figs. 1 and S3c).

45

46 Fig. 1a features our preferred coseismic slip solution with two main patches, the most prominent  
47 downdip the hypocenter, between 21 and 32 km depth with peak value of 3.4 m, and a second one  
48 45 km east-northeast, almost below the coast (peak value of 1.8 m), which differs from a recently  
49 published solution (Melgar et al., 2020) that did not integrate the closest (GPS and strong motion)  
50 data and estimated a static uplift in Huatulco 6 cm higher than ours. Our slip solution explains both  
51 the uplift and seaward displacement there, and shows that no significant slip (i.e. larger than 1 m)  
52 took place offshore (Fig. S3c). Furthermore, it clearly suggests a rupture directivity towards the  
53 north-northeast, essentially downdip from the hypocenter. Two more features stand out from our  
54 model: 1) The rupture ends abruptly updip and very close to the nucleation point. 2) The downdip  
55 slip limit might correspond to the end of the locked segment of the megathrust, as observed for the  
56 2018 Pinotepa Earthquake (Li et al., 2020) and the aftershocks areas of regional interplate  
57 earthquakes (white patches in Fig. 1).

58

59 Whether the 2020 Huatulco earthquake is a repetition of two previous events that occurred in 1928  
60 (Ms 7.6) and 1965 (Ms 7.4) is an important matter that goes beyond the scope of this work.  
61 However, since this question can be addressed by comparing far-field waveforms of the  
62 earthquakes, which are sensitive to the source depth (Chael and Stewart, 1982; Singh et al., 1984),  
63 we performed a supplementary inversion exercise where the interface was shifted 3.5 km upward  
64 to match our relocated hypocentral depth. The inversion yielded similar source characteristics as  
65 described above (Fig. S4) with some differences discussed in the Supplementary Materials that do  
66 not have a significant bearing on any subsequent analysis.

67

## 2.2 The 2020 Oaxaca SSE that preceded the earthquake

Two months before the Huatulco earthquake, on mid-April 2020, three GPS stations in Oaxaca (TNNP, TNNX and OAXA) changed their typical interseismic motion from roughly northeast to southwest, indicating a transient deformation associated with a SSE (light blue section in Figs. 2a and S6a). We used continuous displacement records on 12 permanent GPS stations in Oaxaca belonging to the SSN and Tlalocnet (Cabral-Cano et al., 2018), between September 2019 and the Huatulco earthquake date (Fig. S5) to simultaneously invert for the plate interface coupling (PIC) and any stress-releasing slip episode (e.g. SSEs) in successive time windows using ELADIN (Fig. 2). For these and the next inversions, the 3D plate interface was discretized with coarser subfaults of 10 x 10 km<sup>2</sup>.

Fig. 2e shows the main slow slip patch downdip of the 1978 Puerto Escondido earthquake region, between 25 and 50 km depth, with an equivalent moment magnitude  $M_w$  6.4 ( $M_o = 7.914 \times 10^{18}$  N\*m assuming a shear modulus of 32 GPa). The location and magnitude of this SSE are consistent with previously reported SSEs in Oaxaca (Correa-Mora et al., 2008; Cruz-Atienza et al., 2020; Graham et al., 2016). It is also clear that the SSE did not penetrate the rupture area of the Huatulco earthquake. Instead, we observe a remarkable PIC evolution previous to the event in that area, where the interface decoupled around February-March (Fig. 2d) before getting fully coupled just before the earthquake (i.e. during the strongest SSE phase, Fig. 2e). This can also be seen directly in the GPS time series at the stations closest to the epicenter, such as OXUM and HUAT (Fig. 2a), where we do not observe the SSE southward rebound before the earthquake. In contrast, the displacement trends present a slight acceleration to the north. Something similar occurred in the hypocentral region of the 2018 Pinotepa earthquake 200 km west, where the seismicity rate also increased in the two months preceding the rupture (Cruz-Atienza et al., 2020). We carefully

93 analyzed the foreshock seismicity starting from August 2016 in the hypocentral region of the  
94 Huatulco earthquake using the one-station template-matching procedure introduced by Cruz-  
95 Atienza et al. (2020) using continuous broadband records at the HUIG station (Fig. S7). However,  
96 unlike the observations of the 2018 Pinotepa earthquake, we did not find significant increase in the  
97 seismicity rate before the event that could shed light on the rupture initiation mechanism.

98

99 Although the transient deformation produced by the SSE is noticeable from mid-April, the inter-  
00 SSE displacement trends in some stations started changing well before, around mid-February as  
01 observed in Fig. 2a, suggesting a gradual plate-interface decoupling process at a regional scale  
02 preceding the SSE-induced crustal relaxation, which can be observed in Figs. 2b-2d (and  
03 Supplementary Movie S1). Before this process began (Fig. 2b), the downdip segment of the plate  
04 interface, between 25-50 km, was fully coupled while small SSE episodes were taking place in both  
05 the 2018 Pinotepa earthquake area and up-dip of the Huatulco earthquake rupture zone. In the  
06 following two months, there seems to have been an incipient downdip SSE propagation from south  
07 to north in Pinotepa along with another small relaxation to the east of the area where the long-term  
08 SSE will develop (Supplementary Movie S1 and Figs. 2b-2c). Then, in Fig. 2d we see how the  
09 segment downdip of the 1978 earthquake area is the last one to experience a PIC reduction (i.e. the  
10 interface slip starts accelerating but always below the plate convergence rate) leading to the main  
11 SSE patch occurrence in April-June, the months preceding the earthquake (Fig. 2e). All of these  
12 observations clearly demonstrate the regional-wide preparatory phase for the 2020 Oaxaca SSE.

13

14 A common practice to isolate the deformation associated with slow slip transients is to subtract the  
15 inter-SSE linear trend from the GPS time series. The residual deformation is then assumed to  
16 correspond to the strain released by the SSE (e.g., (Bartlow et al., 2011; Hirose et al., 2014;  
17 Radiguet et al., 2011)). When one does this to invert for the slip at the interface, the preparatory

18 phase of the SSE (i.e. the slow decoupling process preceding the SSE relaxation) is  
19 mapped/interpreted as aseismic slip resulting in an elastic crustal rebound (i.e. a stress drop), which  
20 is not really correct. This assumption leads to systematic overestimations of the SSE related  
21 displacements and thus the equivalent seismic moment with relevant implications in the scaling  
22 properties of slow earthquakes and, more importantly, in the slip budget over several SSE cycles,  
23 which may be significantly underestimated.

### 25 **2.3 Early post-seismic deformation**

26  
27 We inverted the early post-seismic GPS displacements (i.e. the first 2 months discretized in 6 ten-  
28 day windows, Figs. 3a and S6b) produced by the mainshock using the same parameterization for  
29 the ELADIN method as in the previous section. We then assumed that such displacements are only  
30 due to the afterslip on the plate interface, which is a reasonable approximation considering that the  
31 viscoelastic relaxation after a similar thrust event 260 km west, the 2012 (Mw 7.5) Ometepec  
32 earthquake, was negligible in a post-seismic period three times longer (Graham et al., 2014b).

33  
34 Four main observations arise from the afterslip evolution of the Huatulco earthquake (Fig. 3b and  
35 Supplementary Movie S1): (1) the largest afterslip concentrates between 20 and 50 km depth  
36 involving also the main SSE patch occurred before the earthquake (i.e. downdip from the 1978  
37 rupture area) and where previous SSEs have been identified (Fig. S8); (2) the maximum postslip  
38 area completely overlaps with the coseismic rupture area; (3) the afterslip spreads offshore up to  
39 the oceanic trench where most of aftershocks were concentrated; and (4) the afterslip rate reaches  
40 its maximum value of 390 cm/year during the first 10 days following the event.

42 The complete overlap of coseismic and postseismic slip has been observed in the last three interplate  
43 thrust earthquakes ( $M_w > 7$ ) in Oaxaca, the 2012 ( $M_w 7.5$ ) Ometepepec (Graham et al., 2014b); the  
44 2018 ( $M_w 7.2$ ) Pinotepa (Cruz-Atienza et al., 2020) and the 2020 ( $M_w 7.4$ ) Huatulco (this study)  
45 events, indicating that these seismogenic segments of the plate interface, with the depth range  
46 between 10 and 30 km, can release elastic strain energy both seismically and aseismically. The peak  
47 afterslip velocity of the Huatulco event reported above is almost seven times higher than the one of  
48 the Pinotepa earthquake (Supplementary Movie S2) (Cruz-Atienza et al., 2020), suggesting  
49 significant lateral differences in the mechanical properties along the Oaxaca subduction zone.

50

51 The cumulative aseismic moment released during the first two months following the earthquake  
52 was  $1.808 \times 10^{20}$  N\*m, equivalent to a moment magnitude  $M_w 7.44$ , which is 24% larger than the  
53 coseismic moment. The high postseismic/coseismic moment ratio is also a common feature of the  
54 three Oaxaca events mentioned above, that significantly differs from the much lower estimate for  
55 the 2014 ( $M_w 7.4$ ) Papanaoa thrust earthquake in Guerrero, where the aseismic postslip moment was  
56 30% smaller than the corresponding coseismic value (Gualandi et al., 2017).

57

58 One of the most noteworthy features of the postseismic process in the region is that the Huatulco  
59 earthquake postslip did not penetrate the rupture area of the 1978 Puerto Escondido earthquake  
60 (dashed ellipse in Fig. 3b), which remained fully coupled during the two-month period. Unlike the  
61 preseismic phase, the PIC in the 1978 rupture area abruptly increased just after the earthquake  
62 (compare Figs. 2 and 3) suggesting significant dynamic implications in terms of the postseismic  
63 strain accommodation in the region.

64

### 65 **3. Interplate slip-rate evolution in the Oaxaca subduction zone.**

66

67 Before the occurrence of the Huatulco earthquake, a complex sequence of earthquakes and SSEs  
68 took place in an unusual way along the Mexican subduction zone from April 2017 to September  
69 2019 (Cruz-Atienza et al., 2020). During the sequence, the plate interface experienced remarkable  
70 changes of the PIC in the whole megathrust over time (see Supplementary Movies S1 and S2). Fig.  
71 4 summarizes two examples of these remarkably changes where high coupled regions ( $PIC > 0.6$ )  
72 evolve before (green patches) and after (warm color patches) the Pinotepa and Huatulco  
73 earthquakes.

74

75 We analyze the evolution of the aseismic slip along the Oaxaca megathrust before the Huatulco  
76 earthquake by using the slip history inverted by Cruz-Atienza et al. (2020) (from December 2016  
77 to September 2019) and the sequence inverted before the Huatulco earthquake (Fig. 2), linearly  
78 interpolated every 30 days. Fig. 5a shows the evolution of the total aseismic slip on the plate  
79 interface along the trench (i.e. projected into the green lines of Fig. 4) averaged between 10-30 km  
80 depth, which include the segments of the 2018 Pinotepa, 1978 Puerto Escondido and 2020 Huatulco  
81 earthquakes (Fig. 4). Thus, the difference between the final cumulative slip curve and the dashed  
82 line, which represents the expected total displacement of the incoming Cocos plate during the same  
83 period (DeMets et al., 2010), can be interpreted as the slip deficit along the trench in this particular  
84 period.

85

86 We disaggregated the plate interface aseismic total slip into the slip transients associated with SSE  
87 and afterslip, i.e., those events that release elastic strain (Fig. 5b), and the slip that occurs under the  
88 coupling regime, i.e., the interplate creep that produces stress build-up and where the slip velocity  
89 is less than or equal to the plate convergence rate (Fig. 5c). For a given time window, we distinguish  
90 whether a subfault is creeping (in coupling regime) or if it is aseismically slipping releasing stress.  
91 Fig. 5b shows that the afterslip contribution from the Pinotepa earthquake dominates in the region,

92 although there were SSEs in this segment before the earthquake (blue to green areas below the red  
93 curve). There is also a portion of the Huatulco segment where some small SSEs contribute to the  
94 total slip in the plate interface, while this contribution is negligible in the 1978 rupture area.

95  
96 The evolution of creeping (Fig. 5c) reveals strong variations of the slip velocity in different time  
97 intervals along the whole Oaxaca segment, i.e. the interplate coupling significantly changes over  
98 time. Some of the most prominent changes of the PIC occur before and after SSEs (e.g. black  
99 rectangles), as well as in the 1978 earthquake region during the post-seismic deformation of both  
00 the Pinotepa and Huatulco earthquakes, as previously discussed in Figs. 2, 3 and 4.

01  
02 To better analyze the interplate slip-rate variations we extracted the time series of the slip evolution  
03 at four places of the plate interface (dashed circles with radius of 20 km in Fig. 4). Region A, over  
04 the rupture area of the Huatulco earthquake; Region B, over the rupture area of the 1978 Puerto  
05 Escondido earthquake estimated by Mikumo et al. (2002); Region C, updip from the Huatulco  
06 earthquake where most of its aftershocks are located; and Region D, downdip from the rupture area  
07 of the Puerto Escondido earthquake. Figs. 6 and S9a show the evolution of the mean total aseismic  
08 slip (black line), the creeping (yellow line), the relaxing slip (red line) and the PIC (blue line) within  
09 each of the four circular regions.

10  
11 In the Huatulco rupture area (Region A, Fig. 6a), the contribution to the total slip is mainly due to  
12 creeping except for a period after the Mw 8.2 Tehuantepec earthquake, when aseismic stress release  
13 occurred on this patch. This 2017 SSE was indeed triggered by the quasistatic and dynamic stresses  
14 produced by the great Tehuantepec event as demonstrated by (Cruz-Atienza et al., 2020). In this  
15 region, PIC is highly variable over time and correlates remarkably well with the occurrence of  
16 neighboring SSEs in Oaxaca even though these events did not penetrate the region. During the

17 occurrence of such regional SSEs, the PIC gradually decreases down to values of 0.2-0.4 and then  
18 increases in the final stage of the SSEs to recover the relatively high values of 0.7-0.9 observed in  
19 the inter-SSE periods. This behavior is very similar in Region D (Fig. S9a), downdip from the 1978  
20 rupture area, except that PIC starts to recover after the end of the 2019 SSE.

21  
22 In the 1978 rupture area (Region B, Fig. 6b) there is no evidence of aseismic stress release, so the  
23 total slip is only associated with creeping. Although it is not so clear as in Region A, this case is  
24 also characterized by large variations of the PIC that correlate with the occurrence of regional SSEs  
25 and postslip. There is for instance a great variation of the creeping rate before and after the Pinotepa  
26 earthquake, where the PIC raises from  $\sim 0.3$  before the earthquake (i.e. during the final stage of the  
27 2017 Oaxaca SSE) to almost 1.0 (fully coupled) just after the earthquake, and then gradually  
28 decreases to a low PIC value during the corresponding postseismic relaxation. Also notice the sharp  
29 growth of PIC in both regions A and B during the 2020 Oaxaca SSE just before the Huatulco  
30 earthquake.

31  
32 Offshore (and updip) from the Huatulco earthquake (Region C, Fig. 6c) we find a more consistent  
33 low PIC value across the whole studied period with some exceptions after the Tehuantepec  
34 earthquake and just before the initiation of the 2020 SSE. The gap in the PIC curve between  
35 December 2018 and the end of March 2019 means that all subfaults within this region underwent a  
36 SSE. The red curve indicates that there are small and persistent SSEs in this offshore region over  
37 time, which is consistent with the significant afterslip developed there after the Huatulco earthquake  
38 that extended up to the trench. These observations suggest that the frictional properties of this region  
39 are prone to release aseismically a fraction of the accumulated stress.

40

#### 41 **4. Implications of SSEs and PIC changes on the stress built-up**

42

43 Variations in the interplate aseismic slip rate have important implications for both friction (Im et  
44 al., 2020) and the stress build-up along the megathrust. We estimated the Coulomb Failure Stress  
45 (CFS) changes (Nikkhoo and Walter (2015), see Supplementary Materials) produced by the  
46 relaxing slip (SSEs and afterslip) and the interplate coupling to elucidate how the stress evolves  
47 along the Oaxaca segment. For this analysis we have also included the coseismic stresses imparted  
48 by the Pinotepa and Huatulco earthquakes. Figs. 7a and 7b show the average cumulative CFS every  
49 30 days from December 2017 up to the moment of the Huatulco event along the trench for two  
50 different depth ranges encompassing the rupture areas of the 2020 Huatulco (between 20 and 30  
51 km depth) and the 1978 Puerto Escondido (between 10 and 20 km depth) earthquakes. It is  
52 important to note that these estimates of the CFS are the result of stress contributions from the  
53 whole plate interface and not just from the sub-faults delimited by the depth bands.

54

55 As expected, the CFS cumulative rate is highly variable over time and along the trench. For the  
56 deeper band (Fig. 7a), we observe that despite the great variations of the slip-rate on the megathrust,  
57 the CFS in Huatulco always increased up to values ranging from 400 to 800 kPa. The same happens  
58 downdip of the 1978 rupture, where the cumulative CFS is even higher (between 800 kPa and 1  
59 MPa). For the shallower band (Fig. 7b), the CFS decreases and remains negative right updip of the  
60 Huatulco rupture reaching values of  $\sim$ -500 kPa. Such negative values are associated with the stress  
61 shadows produced by neighboring strong coupled segments (e.g. the 1978 earthquake area, Fig. 7c)  
62 and the periodic release of stress by short-term SSEs in this eastern segment (Figs. 2 and 7d). To  
63 the west, in the 1978 rupture area, we find the opposite situation. The CFS always increased to  
64 values between 200 and 500 kPa, which are approximately half of the CFS estimates downdip of  
65 this segment (Fig. 7a).

66

67 Fig. S10 shows both the long-term and inter-SSE time-invariant interplate coupling models  
68 estimated by Radiguet et al. (2016) together with their associated CFS change rate. Both models  
69 produce large stressing rates mainly in the highly coupled segment of the 1978 earthquake region.  
70 However, they also produce large stress shadows in the adjacent less coupled regions (both along-  
71 dip and along-strike) such as in the Pinotepa and Huatulco rupture zones. In contrast, our aseismic  
72 time-evolving slip-rate model predicts a very different scenario. Fig. 8a shows the cumulative CFS  
73 at the time of the Huatulco earthquake including contributions of all aseismic slip processes imaged  
74 in the megathrust during the 3.5 years preceding the event (from December 2016 to June 23, 2020).  
75 A simple inspection reveals large differences in the stress build-up pattern with respect to the time-  
76 invariant models, especially in both the Huatulco and Pinotepa rupture areas, and east-southeast of  
77 the 1978 earthquake zone. The bottom four panels of Fig. 8 show the cumulative (trench-  
78 perpendicular average) CFS along the trench for the same two bands with different depth ranges  
79 analyzed earlier. The left column shows the cumulative CFS at the time of the Huatulco earthquake,  
80 while the right column shows the same quantity plus the coseismic and postseismic stress  
81 increments.

82

83 In the deeper band at the moment and within the rupture area of the Huatulco earthquake (Fig. 8b),  
84 the CFS from our time-evolving slip model (blue area) indicates almost double the CFS predicted  
85 by the inter-SSE coupling model (yellow area) and more than twice in the downdip region of the  
86 1978 rupture area. On the contrary, the long-term coupling model (orange area) predicts negative  
87 CFS values in Huatulco (i.e. no earthquake potential) and low positive values in the downdip region  
88 of the 1978 rupture. When adding the CFS imparted by the Huatulco earthquake and its postseismic  
89 afterslip (Fig. 8e), our estimate doubles up right downdip of the 1978 rupture area, from about 800  
90 kPa to over 1.8 MPa. A significant fraction of this value is due to the persistently high coupling in  
91 this region throughout the post-seismic phase (Fig. 3). This large segment west of the Huatulco

92 rupture (Region D in Fig. 8d) is then very prone to a future earthquake, as has occurred in  
93 neighboring regions over the deep part of the locked zone, where the last two interplate earthquakes  
94 in Oaxaca (the Pinotepa and Huatulco events) took place with most of their seismic moment  
95 released below 20 km (Li et al., 2020).

96

97 In the shallower band, the three models predict similar CFS values over the 1978 rupture area before  
98 the Huatulco rupture (Fig. 8c), although the inter-SSE model gives much higher values in the  
99 eastern part of the main patch. Between the 1978 and Huatulco ruptures areas, only our short-term  
00 model predicts a CFS deficit, which is fully compensated (reaching positive values around 800 kPa)  
01 by the coseismic and postseismic deformations produced by the Huatulco earthquake (Fig. 8f).

02

03 We can therefore distinguish three major differences between our time-evolving CFS estimates,  
04 which integrate all contributions from relaxing slip (SSEs and afterslip) and coupled regions in  
05 Oaxaca, and both time-invariant coupling models: (1) very high stress concentration over the  
06 rupture area of the Huatulco earthquake predicted only by our model, (2) absolute CFS values  
07 between 20 and 30 km depth at least twice as high in our model, and (3) a large stress shadow zone  
08 updip the Huatulco rupture that is absent in both time-invariant models.

09

10 We now analyze in depth the CFS stress evolution in the Huatulco and 1978 rupture areas (within  
11 the circular regions A and B, Fig. 8a) given by our time-evolving interplate slip-rate model. Figs  
12 9a and 9b show the total CFS evolution in both regions (black curves) together with the linear  
13 predictions given by the time-invariant coupling models of (Radiguet et al., 2016) (green lines). To  
14 assess which slip process dominates the stress build-up, we also disaggregated the total CFS into  
15 the stress contributions produced by regions in coupling regime only (yellow curves) and by the  
16 relaxing slip only (red curves).

17

18 In the Huatulco rupture zone (Region A, Fig. 9a) our model shows a sustained growth of the total  
19 CFS during the 3.5 years prior to the rupture, reaching values close to 700 kPa and where 80% of  
20 the stress contribution comes from interface regions in coupling regime. The remaining 20% is  
21 mainly associated with the contribution of the SSE occurred following the 2017 Tehuantepec  
22 earthquake. In contrast, the time-invariant long-term coupling model predicts a sustained decrease  
23 of CFS that implies a continuous reduction of the earthquake potential. On the other hand, while  
24 the inter-SSE time-invariant model predicts a growth of the CFS, the final value is about one third  
25 of what our model yields. Since the Huatulco earthquake took place, it seems that our time-evolving  
26 slip-rate model and its associated CFS clearly represents a more realistic description of the actual  
27 megathrust processes than any of the time-invariant coupling models analyzed here. This is also  
28 easily seen by comparing our CFS estimates in the hypocentral region at the time of the earthquake  
29 (Supplementary Movie S1 and Fig. 8a) with those produced by the time-invariant coupling models  
30 (Fig. S10).

31

32 Considering the 1978 Puerto Escondido rupture zone (Region B, Fig. 9b), although our model  
33 predicts an effective CFS increase of about 400 kPa at the time of the Huatulco earthquake, it also  
34 reveals significant temporal variations that are primarily controlled by the stress contributions from  
35 interface regions in a coupling regime. At that time, the stress produced by SSEs is 100 kPa, which  
36 represents ~25% of the total CFS. For this specific region, while the inter-SSE time-invariant model  
37 predicts a cumulative stress that is almost twice our model's prediction, the long-term time-  
38 invariant model is close to our time-evolving cumulative value. When integrating the stress  
39 contributions from both the coseismic and postseismic slip of the Huatulco earthquake, then our  
40 stress estimate gets close to the inter-SSE prediction with high CFS values around 800 kPa.

41

42 Fig. S11 presents the contributions to the CFS of both relaxing slip and coupling separately.  
43 Although in very different proportions, both contributions promote an increase in earthquake  
44 potential in the rupture areas of the Huatulco and 1978 earthquakes. Figs. 9c and 9d show the  
45 percentages of these contributions only where the total CFS is positive in Fig. 8a (i.e. where there  
46 was an effective increase of the earthquake potential). We can see that the rupture zones of the  
47 Huatulco and 1978 earthquakes (Regions A and B, Figs. 9a and 9b) are actually representative of  
48 the accumulation and partitioning of stresses between 20-35 km depth in all but the western segment  
49 of the region. We can also see that although most of the accumulated stress (i.e. ~75-85%) was  
50 generated by coupled interface regions, 15-25% was due to the SSEs and the afterslip (of the 2018  
51 Pinotepa earthquake) occurring in the region over the 3.5 years period.

52

## 53 **5. Discussion**

54

55 The segment of the plate interface where the Huatulco earthquake ruptured has been characterized  
56 with moderate coupling (Fig. S10) (Radiguet et al., 2016; Rousset et al., 2016). Previous M7 class  
57 interplate earthquakes have occurred very close to it, such as the 1965 and 1928 events, suggesting  
58 a possible reactivation of the same asperity over time (Chael and Stewart, 1982; Singh et al., 1984).  
59 Historical data also suggest that two older, probably thrust earthquakes with magnitude larger than  
60 7 occurred nearby in 1870 and 1801 (Suárez et al., 2020). Assuming that all these events broke the  
61 same plate interface patch, their average return period would be  $\sim 55 \pm 13$  years. In this region also  
62 occurred the Mw  $\sim 8.6$  San Sixto earthquake in 1787 over a  $\sim 300$  km along-strike segment  
63 producing a great tsunami offshore Oaxaca (Ramírez-Herrera et al., 2020; Suárez and Albinì, 2009).  
64 Such event must have involved the rupture of several locked segments along the Oaxaca megathrust  
65 including offshore shallow portions of the plate interface to generate the mega-tsunami. Whether  
66 M8+ events may repeat depends, among other factors, on the interplate friction and constructive

67 stress interaction between different locked and unlocked fault segments (Kaneko et al., 2010;  
68 Kaneko et al., 2018), which continuously change over time. Recent laboratory experiments and  
69 theoretical fault models strongly suggest that the friction is a sensitive function of the interplate slip  
70 velocity where SSEs take place (Im et al., 2020). Then, since the slip velocity changes over time,  
71 these variations should be essential for the dynamic stability of the megathrust because of both their  
72 frictional counterparts and the associated stress changes documented here for the Oaxaca  
73 subduction zone. To have an insight into the actual earthquake potential (e.g. to assess whether  
74 adjacent locked segments are likely to break jointly to produce a much larger event) it is therefore  
75 necessary a proper and continuous quantification of the stress accumulation as proposed here.  
76 Monitoring the interplate slip-rate continuously might also allow us to constrain the evolution of  
77 the frictional parameters that determine the slip stability regime on the megathrust.

78

79 An interesting feature of the Huatulco earthquake is that rupture did not propagate into the adjacent  
80 updip segment (above ~17 km depth) that should also be locked. Impeding the rupture propagation  
81 into that segment might be associated with the interface geometry (e.g. due to subducted plate reliefs  
82 as recently proposed in the Guerrero seismic gap (Plata-Martínez et al., 2020)), the frictional  
83 conditions and/or, as shown in this investigation, with the existence of a significantly-large stress  
84 barrier due to both the stress shadow produced by nearby strongly coupled zones and persistent  
85 small SSE occurring updip. The spatial distribution of aftershocks during the first 50 days following  
86 the Huatulco event is clearly shifted updip (about 30 km) from the rupture area, where the afterslip  
87 developed and the CFS strongly increased. Only very few aftershocks lie within the main slip patch,  
88 indicating an effective stress release within the most of the rupture area, which is consistent with  
89 other M7 class earthquakes observed worldwide (Wetzler et al., 2018). Furthermore, the earthquake  
90 nucleation in the shallowest part of the rupture zone and northward propagation can also be  
91 explained by our model due to the localized increments of CFS right in the nucleation zone over

92 the six months prior to the earthquake (Supplementary Movie S1) and the longer-term stress  
93 accumulation downdip the hypocenter (Figs. 7a and 8a), respectively.

94

95 We find that strongly coupled regions in Oaxaca are highly variable in space and time before and  
96 after the occurrence of the Pinotepa and Huatulco earthquakes. These remarkable PIC variations  
97 might be associated with abrupt changes in the mechanical properties of the fault zone materials  
98 induced by the dynamic perturbations of the seismic waves from the earthquakes (Cruz-Atienza et  
99 al., 2020; Materna et al., 2019). Furthermore, we observed that the PIC changes are somehow linked  
00 to nearby SSEs that occur in the region (Figs. 6a and S9a). To explain these short-term variations  
01 of the PIC at seismogenic depths, we favor models involving fluctuations of fluid pressure as  
02 proposed for the long-term SSEs in the Guerrero subduction zone (Cruz-Atienza et al., 2018), in  
03 southern Cascadia (Materna et al., 2019) and the Hikurangi subduction zone (Warren-Smith et al.,  
04 2019). Recently, models evoking the fault-valving concept show overpressure pulses migrating  
05 upward along the fault as the permeability evolves in the fault zone (Cruz-Atienza et al., 2018;  
06 Shapiro et al., 2018; Zhu et al., 2020). These transient changes in pore pressure may lead to large  
07 variations of the fault strength as high as ~10-20 MPa (Zhu et al., 2020), which makes this  
08 mechanism a plausible candidate to explain the strong PIC variations in the seismogenic zone of  
09 Oaxaca during the occurrence of SSEs and earthquakes.

10

11 Earthquake potential depends on the state of stress along the subduction zone that, as shown here,  
12 is a function of different evolving processes taking place from the trench to its deep portion where  
13 the plates mechanical interaction ceases. The stress build-up therefore changes over time and space  
14 in a complex way, so does the earthquake potential. Time-invariant estimates of the interplate  
15 coupling are often used to identify seismogenic segments that are prone to large earthquakes (Chlieh  
16 et al., 2008; Loveless and Meade, 2011; Moreno et al., 2010; Perfettini et al., 2010). However,  
17 while these estimates are certainly useful on a large spatial and temporal scale, they do not provide

18 a reliable picture of the earthquake potential associated with smaller ( $7 < M < 8.5$ ) but potentially  
19 devastating ruptures that occur more frequently, as shown in this work for the Oaxaca megathrust.

20

21 Our results indicate that continuously monitoring the interplate slip velocity provides a better  
22 reconstruction of the stress development on the seismogenic region. Systematic and simultaneous  
23 observation of PIC and the relaxing slip (SSE and afterslip) over the plate interface is thus very  
24 relevant to evaluate theoretical predictions of the interface dynamics, which is our leading approach  
25 to understand the underlying physics in subduction systems.

26

## 27 **6. Conclusions**

28

29 We analyzed the interplate slip-rate evolution during 3.5 years in the Oaxaca subduction zone  
30 including the pre-seismic, coseismic and post-seismic phases associated with the June 23, 2020 Mw  
31 7.4 Huatulco earthquake to understand how the different slip processes contribute to the plate-  
32 interface stress accumulation in the region. We found that the main rupture area of the Huatulco  
33 earthquake extends between 20 and 30 km depth with two main and compact slip patches, the most  
34 prominent north the hypocenter and a much smaller close to the coast, east-northeast of the  
35 hypocenter. The 2020 SSE that occurred before the earthquake did not penetrate the rupture area  
36 and was preceded by a gradual interface decoupling process at a regional scale, including the  
37 maximum SSE slip area. During the two months preceding to the earthquake, when the 2020 SSE  
38 developed, the Huatulco earthquake rupture area became fully locked. Our slip inversions indicate  
39 that the two-month earthquake afterslip overlapped the whole coseismic rupture area and  
40 propagated both to the trench and to the northwest, where most of aftershocks happened and where  
41 the 2020 SSE was developing as well as previous SSEs have occurred in the region, respectively.  
42 During the post-seismic phase, the rupture area of the 1978 Puerto Escondido earthquake became

43 and remained fully coupled. The interplate slip-rate evolution in Oaxaca during the 3.5 years  
44 preceding the Huatulco earthquake shows that the PIC in the megathrust seismogenic region is  
45 highly variable in time and space, and that the PIC reductions over the Huatulco and the 1978  
46 rupture areas are well correlated with the occurrence of SSEs further downdip, clearly suggesting  
47 a physical relationship between both processes. We found that both stress-relaxing aseismic slip  
48 events and megathrust coupling changes produced a region of high stress accumulation where the  
49 main asperity of the Huatulco earthquake broke as well as a shallow stress deficit region that  
50 probably impeded the updip propagation of the earthquake. Our results suggest that  
51 continuous monitoring of the interplate aseismic slip-rate and its CFS counterpart provides a better  
52 estimation of the earthquake potential on locked seismogenic regions than predictions given by  
53 time-independent interplate coupling models. Finally, the stress imparted during the coseismic and  
54 postseismic phases of the Huatulco earthquake on the 1978 rupture area make it a region very prone  
55 to the next earthquake in the nearest future, which is consistent with the ~50 years earthquake return  
56 period in the Oaxaca region.

57

#### 58 **Declaration on competing or conflict of interest**

59 The authors have no competing or conflict of interest in what is expressed in this manuscript.

#### 60 **CRedit authorship contribution statement**

61 **C. Villafuerte:** Conceptualization, Methodology, Investigation, Formal Analysis, Writing-

62 Original Draft, Visualization. **V.M. Cruz-Atienza:** Conceptualization, Methodology,

63 Investigation, Formal Analysis, Visualization, Writing-Review & Editing, Supervision. **J.**

64 **Tago:** Methodology, Investigation, Software, Validation, Review & Editing. **D. Solano-**

65 **Rojas:** Investigation, Validation, Data processing, Review & Editing **R. Garza-Girón:**

66 Investigation, Visualization, Data processing, Review & Editing **S.I. Franco:** Data processing,

67 Editing. **L.A. Dominguez:** Investigation, Editing. **V. Kostoglodov:** Investigation, Review &  
68 Editing.

69

## 70 **Acknowledgments**

71 We are grateful for the outstanding technical support of Eduardo Murrieta and Luciano Díaz. We  
72 also thank Shri Krishna Singh, Arturo Iglesias and Gerardo Suárez for fruitful discussion; the  
73 Servicio Sismológico Nacional (SSN) and the Servicio Mareográfico Nacional (SMN), both from  
74 UNAM, for the GPS, strong motion and tide gauge data, as well as all their technicians. This work  
75 was supported by CONACyT grants 6471 and 255308, UNAM-PAPIIT grants IN113814,  
76 IG100617 and IG100921, JICA-JST SATREPS-UNAM grant 15543611, UNAM-DGTIC grant  
77 LANCAD-312 and the graduate school scholarships by the Consejo Nacional de Ciencia y  
78 Tecnología (CONACyT).

79

## 80 **References**

81

82 Bartlow, N.M., Miyazaki, S.i., Bradley, A.M., Segall, P., 2011. Space-time correlation of slip and  
83 tremor during the 2009 Cascadia slow slip event. *Geophysical Research Letters* 38.

84 Beroza, G.C., Ide, S., 2011. Slow Earthquakes and Nonvolcanic Tremor. *Annual Review of Earth  
85 and Planetary Sciences* 39, 271-296.

86 Cabral-Cano, E., Pérez-Campos, X., Márquez-Azúa, B., Sergeeva, M.A., Salazar-Tlaczani, L.,  
87 DeMets, C., Adams, D., Galetzka, J., Hodgkinson, K., Feaux, K., Serra, Y.L., Mattioli,  
88 G.S., Miller, M., 2018. TLALOCNet: A Continuous GPS-Met Backbone in Mexico for  
89 Seismotectonic and Atmospheric Research. *Seismological Research Letters* 89, 373-381.

- 90 Chael, E.P., Stewart, G.S., 1982. Recent large earthquakes along the Middle American Trench and  
91 their implications for the subduction process. *Journal of Geophysical Research: Solid*  
92 *Earth* 87, 329-338.
- 93 Chlieh, M., Avouac, J.P., Sieh, K., Natawidjaja, D.H., Galetzka, J., 2008. Heterogeneous coupling  
94 of the Sumatran megathrust constrained by geodetic and paleogeodetic measurements.  
95 *Journal of Geophysical Research: Solid Earth* 113.
- 96 Correa-Mora, F., DeMets, C., Cabral-Cano, E., Marquez-Azua, B., Diaz-Molina, O., 2008.  
97 Interplate coupling and transient slip along the subduction interface beneath Oaxaca,  
98 Mexico. *Geophysical Journal International* 175, 269-290.
- 99 Cotte, N., Walpersdorf, A., Kostoglodov, V., Vergnolle, M., Santiago, J.-A., Campillo, M., 2009.  
00 Anticipating the Next Large Silent Earthquake in Mexico. *Eos, Transactions American*  
01 *Geophysical Union* 90, 181-182.
- 02 Cruz-Atienza, V.M., Tago, J., Villafuerte, C., Wei, M., Garza-Girón, R., Dominguez, L.A.,  
03 Kostoglodov, V., Nishimura, T., Franco, S., Real, J., 2020. Short-Term Interaction  
04 between Silent and Devastating Earthquakes in Mexico. *Earth and Space Science Open*  
05 *Archive*, 53.
- 06 Cruz-Atienza, V.M., Villafuerte, C., Bhat, H.S., 2018. Rapid tremor migration and pore-pressure  
07 waves in subduction zones. *Nature Communications* 9, 2900.
- 08 Delorey, A.A., Chao, K., Obara, K., Johnson, P.A., 2015. Cascading elastic perturbation in Japan  
09 due to the 2012 *M<sub>w</sub>* 8.6 Indian Ocean earthquake. *Science*  
10 *Advances* 1, e1500468.
- 11 DeMets, C., Gordon, R.G., Argus, D.F., 2010. Geologically current plate motions. *Geophysical*  
12 *Journal International* 181, 1-80.
- 13 Graham, S., DeMets, C., Cabral-Cano, E., Kostoglodov, V., Rousset, B., Walpersdorf, A., Cotte,  
14 N., Lasserre, C., McCaffrey, R., Salazar-Tlaczani, L., 2016. Slow Slip History for the

15 MEXICO Subduction Zone: 2005 Through 2011. *Pure and Applied Geophysics* 173,  
16 3445-3465.

17 Graham, S.E., DeMets, C., Cabral-Cano, E., Kostoglodov, V., Walpersdorf, A., Cotte, N.,  
18 Brudzinski, M., McCaffrey, R., Salazar-Tlaczani, L., 2014a. GPS constraints on the 2011–  
19 2012 Oaxaca slow slip event that preceded the 2012 March 20 Ometepec earthquake,  
20 southern Mexico. *Geophysical Journal International* 197, 1593-1607.

21 Graham, S.E., DeMets, C., Cabral-Cano, E., Kostoglodov, V., Walpersdorf, A., Cotte, N.,  
22 Brudzinski, M., McCaffrey, R., Salazar-Tlaczani, L., 2014b. GPS constraints on the  
23 Mw = 7.5 Ometepec earthquake sequence, southern Mexico: coseismic and post-seismic  
24 deformation. *Geophysical Journal International* 199, 200-218.

25 Gualandi, A., Perfettini, H., Radiguet, M., Cotte, N., Kostoglodov, V., 2017. GPS deformation  
26 related to the Mw 7.3, 2014, Papanao earthquake (Mexico) reveals the aseismic behavior  
27 of the Guerrero seismic gap. *Geophysical Research Letters* 44, 6039-6047.

28 Heki, K., Mitsui, Y., 2013. Accelerated pacific plate subduction following interplate thrust  
29 earthquakes at the Japan trench. *Earth and Planetary Science Letters* 363, 44-49.

30 Hirose, H., Matsuzawa, T., Kimura, T., Kimura, H., 2014. The Boso slow slip events in 2007 and  
31 2011 as a driving process for the accompanying earthquake swarm. *Geophysical Research*  
32 *Letters* 41, 2778-2785.

33 Im, K., Saffer, D., Marone, C., Avouac, J.-P., 2020. Slip-rate-dependent friction as a universal  
34 mechanism for slow slip events. *Nature Geoscience* 13, 705-710.

35 Kaneko, Y., Avouac, J.-P., Lapusta, N., 2010. Towards inferring earthquake patterns from geodetic  
36 observations of interseismic coupling. *Nature Geoscience* 3, 363-369.

37 Kaneko, Y., Wallace, L.M., Hamling, I.J., Gerstenberger, M.C., 2018. Simple Physical Model for  
38 the Probability of a Subduction- Zone Earthquake Following Slow Slip Events and

39 Earthquakes: Application to the Hikurangi Megathrust, New Zealand. *Geophysical*  
40 *Research Letters* 45, 3932-3941.

41 Lay, T., Kanamori, H., 1981. An Asperity Model of Large Earthquake Sequences, *Earthquake*  
42 *Prediction*, pp. 579-592.

43 Li, Y., Shan, X., Zhu, C., Qiao, X., Zhao, L., Qu, C., 2020. Geodetic Model of the 2018 Mw 7.2  
44 Pinotepa, Mexico, Earthquake Inferred from InSAR and GPS Data. *Bulletin of the*  
45 *Seismological Society of America* 110, 1115-1124.

46 Loveless, J.P., Meade, B.J., 2011. Spatial correlation of interseismic coupling and coseismic rupture  
47 extent of the 2011 MW = 9.0 Tohoku-oki earthquake. *Geophysical Research Letters* 38.

48 Materna, K., Bartlow, N., Wech, A., Williams, C., Bürgmann, R., 2019. Dynamically Triggered  
49 Changes of Plate Interface Coupling in Southern Cascadia. *Geophysical Research Letters*  
50 46, 12890-12899.

51 Melgar, D., Ruiz-Angulo, A., Pérez-Campos, X., Crowell, B.W., Xu, X., Cabral-Cano, E.,  
52 Brudzinski, M.R., Rodriguez-Abreu, L., 2020. Energetic Rupture and Tsunamigenesis  
53 during the 2020 Mw 7.4 La Crucecita, Mexico Earthquake. *Seismological Research*  
54 *Letters*.

55 Melnick, D., Moreno, M., Quinteros, J., Baez, J.C., Deng, Z., Li, S., Oncken, O., 2017. The super-  
56 interseismic phase of the megathrust earthquake cycle in Chile. *Geophysical Research*  
57 *Letters* 44, 784-791.

58 Mikumo, T., Yagi, Y., Singh, S.K., Santoyo, M.A., 2002. Coseismic and postseismic stress changes  
59 in a subducting plate: Possible stress interactions between large interplate thrust and  
60 intraplate normal-faulting earthquakes. *Journal of Geophysical Research: Solid Earth* 107,  
61 ESE 5-1-ESE 5-12.

62 Moreno, M., Melnick, D., Rosenau, M., Bolte, J., Klotz, J., Echtler, H., Baez, J., Bataille, K., Chen,  
63 J., Bevis, M., Hase, H., Oncken, O., 2011. Heterogeneous plate locking in the South–

64 Central Chile subduction zone: Building up the next great earthquake. *Earth and Planetary*  
65 *Science Letters* 305, 413-424.

66 Moreno, M., Rosenau, M., Oncken, O., 2010. 2010 Maule earthquake slip correlates with pre-  
67 seismic locking of Andean subduction zone. *Nature* 467, 198-202.

68 Nikkhoo, M., Walter, T.R., 2015. Triangular dislocation: an analytical, artefact-free solution.  
69 *Geophysical Journal International* 201, 1119-1141.

70 Obara, K., Kato, A., 2016. Connecting slow earthquakes to huge earthquakes. *Science* 353, 253-  
71 257.

72 Perfettini, H., Avouac, J.-P., Tavera, H., Kositsky, A., Nocquet, J.-M., Bondoux, F., Chlieh, M.,  
73 Sladen, A., Audin, L., Farber, D.L., Soler, P., 2010. Seismic and aseismic slip on the  
74 Central Peru megathrust. *Nature* 465, 78-81.

75 Plata-Martínez, R., Ide, S., Shinohara, M., Garcia, E., Mizuno, N., Dominguez, L.A., Taira, T.a.,  
76 Yamashita, Y., Toh, A., Yamada, T., Real, J., Husker, A., Cruz-Atienza, V.M., Ito, Y.,  
77 2020. Shallow slow earthquakes to decipher future catastrophic earthquakes in the  
78 Guerrero seismic gap. In review at *Nature Communications*.

79 Radiguet, M., Cotton, F., Vergnolle, M., Campillo, M., Valette, B., Kostoglodov, V., Cotte, N.,  
80 2011. Spatial and temporal evolution of a long term slow slip event: the 2006 Guerrero  
81 Slow Slip Event. *Geophysical Journal International* 184, 816-828.

82 Radiguet, M., Perfettini, H., Cotte, N., Gualandi, A., Valette, B., Kostoglodov, V., Lhomme, T.,  
83 Walpersdorf, A., Cabral Cano, E., Campillo, M., 2016. Triggering of the 2014 Mw7.3  
84 Papanoa earthquake by a slow slip event in Guerrero, Mexico. *Nature Geoscience* 9, 829-  
85 833.

86 Ramírez-Herrera, M.-T., Corona, N., Cerny, J., Castillo-Aja, R., Melgar, D., Lagos, M.,  
87 Goguitchaichvili, A., Machain, M.L., Vazquez-Caamal, M.L., Ortuño, M., Caballero, M.,

88 Solano-Hernandez, E.A., Ruiz-Fernández, A.-C., 2020. Sand deposits reveal great  
89 earthquakes and tsunamis at Mexican Pacific Coast. *Scientific Reports* 10, 11452.

90 Rousset, B., Lasserre, C., Cubas, N., Graham, S., Radiguet, M., DeMets, C., Socquet, A., Campillo,  
91 M., Kostoglodov, V., Cabral-Cano, E., Cotte, N., Walpersdorf, A., 2016. Lateral  
92 Variations of Interplate Coupling along the Mexican Subduction Interface: Relationships  
93 with Long-Term Morphology and Fault Zone Mechanical Properties. *Pure and Applied*  
94 *Geophysics* 173, 3467-3486.

95 Saffer, D.M., Wallace, L.M., 2015. The frictional, hydrologic, metamorphic and thermal habitat of  
96 shallow slow earthquakes. *Nature Geoscience* 8, 594-600.

97 Segall, P., Bradley, A.M., 2012. Slow-slip evolves into megathrust earthquakes in 2D numerical  
98 simulations. *Geophysical Research Letters* 39.

99 Shapiro, N.M., Campillo, M., Kaminski, E., Vilotte, J.-P., Jaupart, C., 2018. Low-Frequency  
00 Earthquakes and Pore Pressure Transients in Subduction Zones. *Geophysical Research*  
01 *Letters* 45, 11,083-011,094.

02 Singh, S.K., Astiz, L., Havskov, J., 1981. Seismic gaps and recurrence periods of large earthquakes  
03 along the Mexican subduction zone: A reexamination. *Bulletin of the Seismological*  
04 *Society of America* 71, 827-843.

05 Singh, S.K., Dominguez, T., Castro, R., Rodriguez, M., 1984. P waveform of large, shallow  
06 earthquakes along the Mexican subduction zone. *Bulletin of the Seismological Society of*  
07 *America* 74, 2135-2156.

08 Suárez, G., Albin, P., 2009. Evidence for Great Tsunamigenic Earthquakes (M 8.6) along the  
09 Mexican Subduction Zone. *Bulletin of the Seismological Society of America* 99, 892-896.

10 Suárez, G., Ruiz-Barón, D., Chico-Hernández, C., Zúñiga, F.R., 2020. Catalog of Preinstrumental  
11 Earthquakes in Central Mexico: Epicentral and Magnitude Estimations Based on  
12 Macroseismic Data. *Bulletin of the Seismological Society of America*.

13 Tago, J., Cruz-Atienza, V.M., Villafuerte, C., Nishimura, T., Kostoglodov, V., Real, J., Ito, Y.,  
14 2020. Adjoint Slip Inversion under a Constrained Optimization Framework: Revisiting the  
15 2006 Guerrero Slow Slip Event. *Earth and Space Science Open Archive*, 34.

16 Uchida, N., Iinuma, T., Nadeau, R.M., Bürgmann, R., Hino, R., 2016. Periodic slow slip triggers  
17 megathrust zone earthquakes in northeastern Japan. *Science* 351, 488-492.

18 Voss, N., Dixon, T.H., Liu, Z., Malservisi, R., Protti, M., Schwartz, S., 2018. Do slow slip events  
19 trigger large and great megathrust earthquakes? *Science Advances* 4, eaat8472.

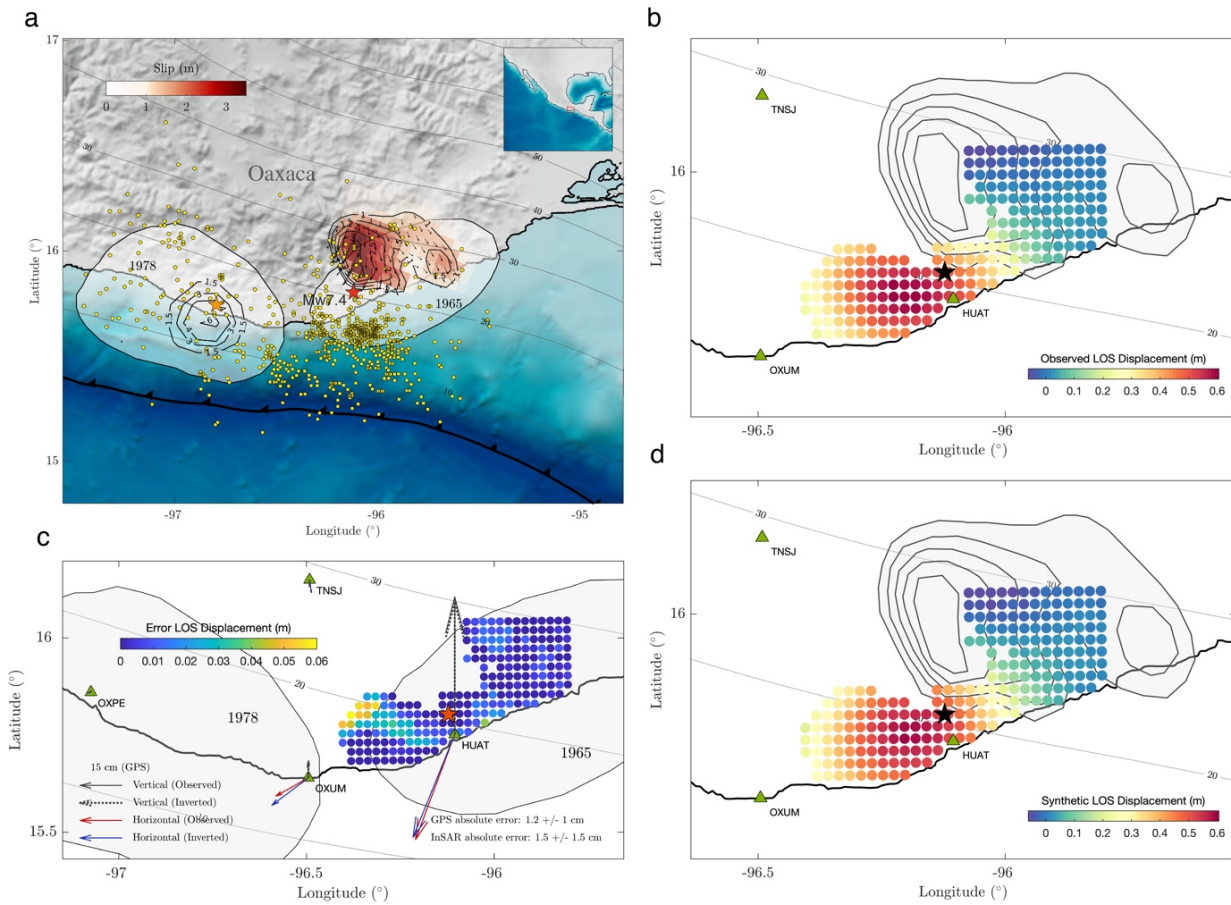
20 Warren-Smith, E., Fry, B., Wallace, L., Chon, E., Henrys, S., Sheehan, A., Mochizuki, K.,  
21 Schwartz, S., Webb, S., Lebedev, S., 2019. Episodic stress and fluid pressure cycling in  
22 subducting oceanic crust during slow slip. *Nature Geoscience* 12, 475-481.

23 Wetzler, N., Lay, T., Brodsky, E.E., Kanamori, H., 2018. Systematic deficiency of aftershocks in  
24 areas of high coseismic slip for large subduction zone earthquakes. *Science Advances* 4,  
25 eaao3225.

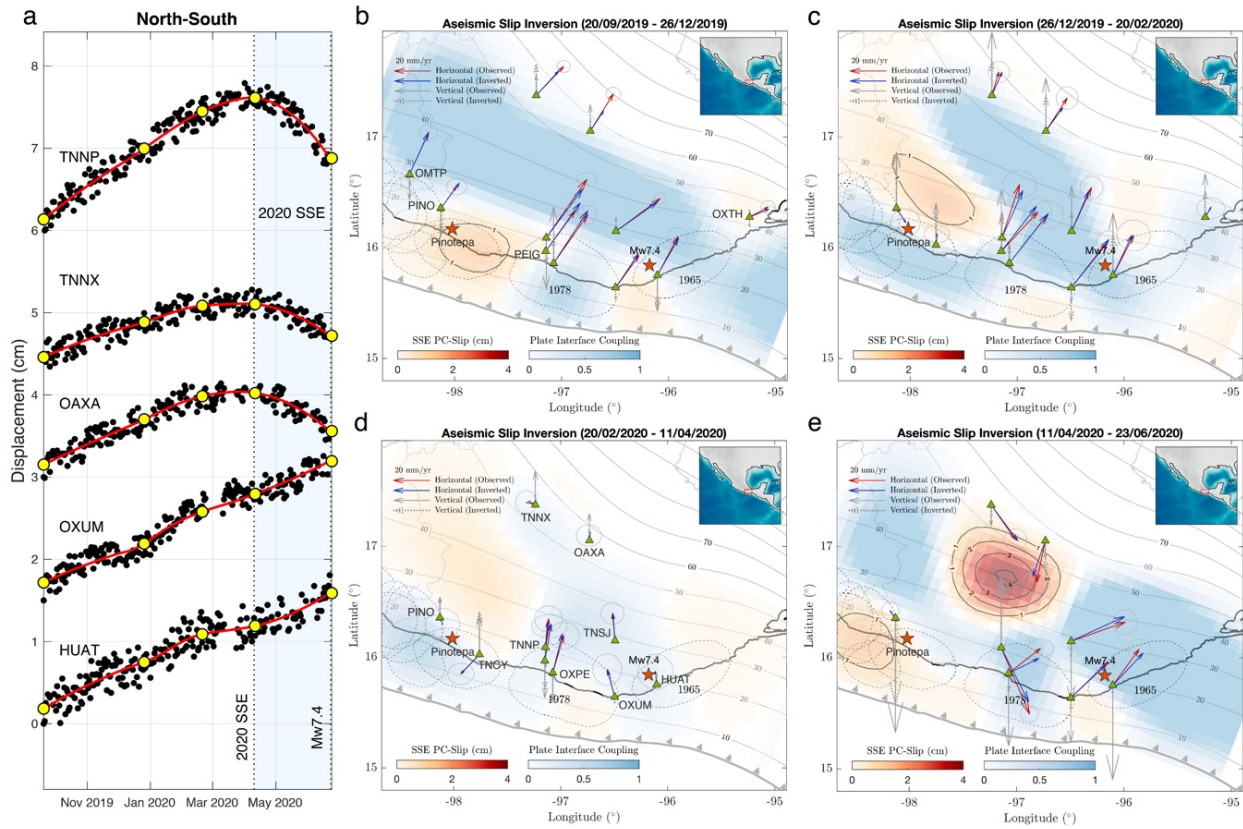
26 Zhu, W., Allison, K.L., Dunham, E.M., Yang, Y., 2020. Fault valving and pore pressure evolution  
27 in simulations of earthquake sequences and aseismic slip. *Nature Communications* 11,  
28 4833.

29

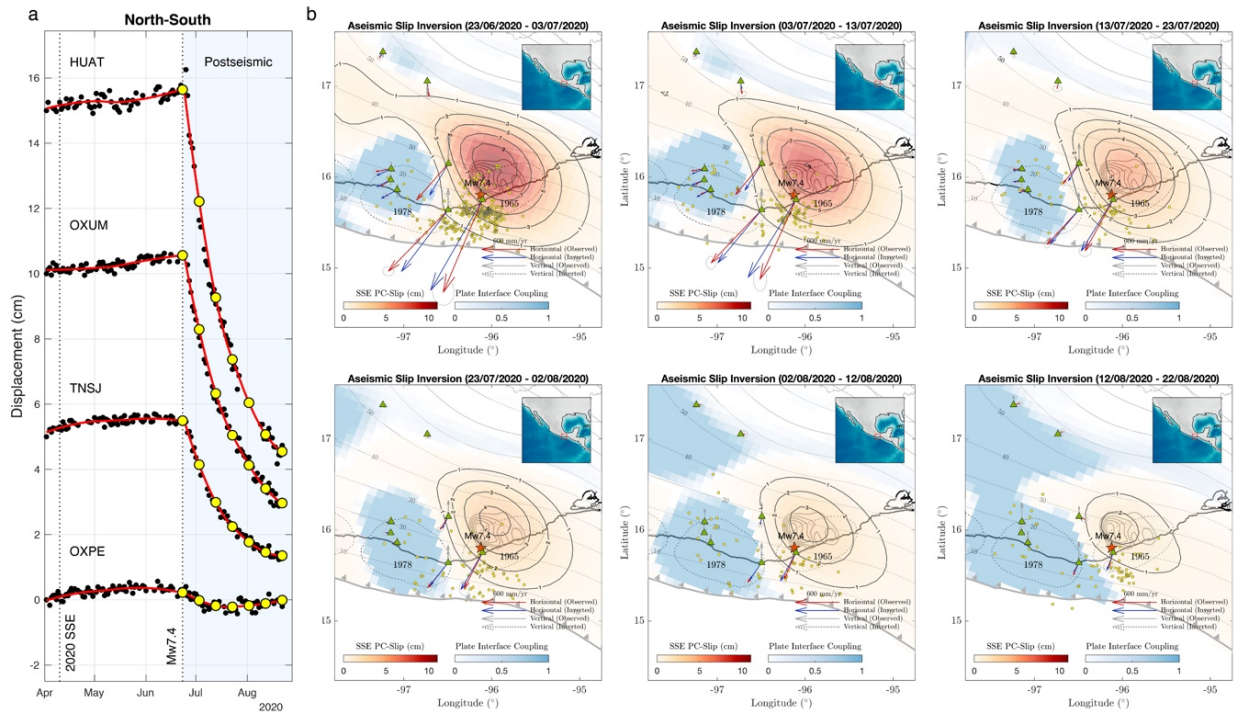
## Figures



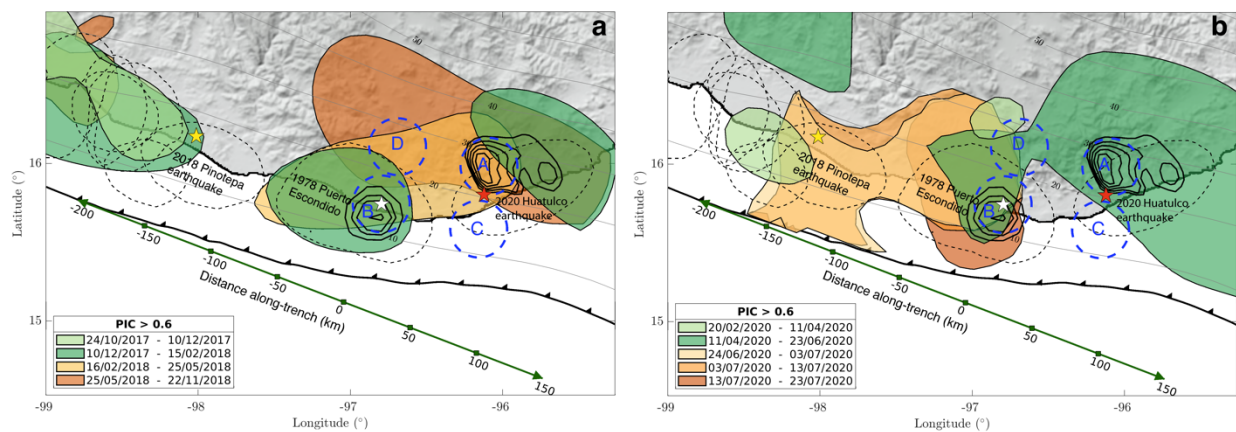
31  
32  
33  
34 **Fig. 1** Coseismic slip inversion results for the 2020 Mw 7.4 Huatulco earthquake. **a** Red colored region with  
35 black contours indicates the slip on the plate interface for our preferred joint GPS and InSAR slip inversion.  
36 Red and orange stars indicate the epicenters of the Huatulco and the 1978 Puerto Escondido earthquakes,  
37 respectively. Black contours around the 1978 Puerto Escondido hypocenter represent the 1.5, 3, 4 and 6 m  
38 slip isolines from Mikumo et al. (2002). White shaded patches show the aftershock areas of the historic  
39 interplate earthquakes in 1965 and 1978. Yellow dots depict the 50 days aftershocks reported by the SSN.  
40 Gray contours indicate the iso-depths of the 3D plate interface used for the slip inversions in this study. **b**  
41 and **d** show the observed and synthetic line of sight (LOS) displacements, respectively. **c** Misfit between  
42 observed and predicted LOS displacement and GPS surface displacements. Red and blue arrows show the  
43 observed and synthetic horizontal displacements from the GPS data. Continuous and dashed arrows indicate  
44 the observed and synthetic vertical displacement, respectively.  
45



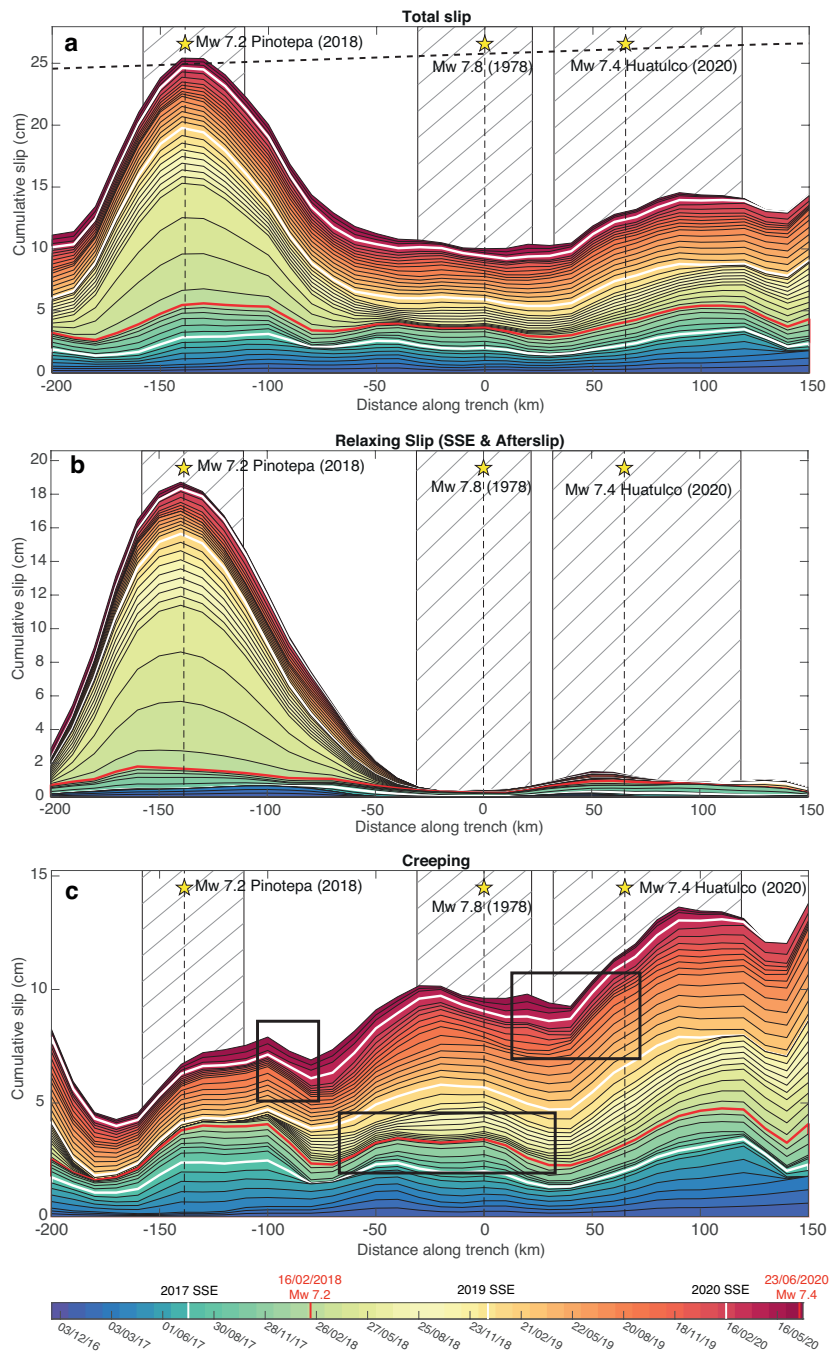
46  
 47 **Fig. 2** GPS inversions of the pre-seismic deformation period during the two months preceding the Huatulco  
 48 earthquake. **a** North-south displacement GPS time series in 5 selected stations. Yellow dots indicate the start  
 49 and the end of the four time-windows used for the slip inversions shown in **b-e**. **b-e** Aseismic slip inversion  
 50 for the 9 months deformation preceding the Huatulco earthquake. Red star depicts the epicenter of the  
 51 earthquake. Slip contours are in centimeters. Dashed regions are the aftershock areas of historic interplate  
 52 earthquakes. Red and blue arrows show the observed and synthetic horizontal displacements and the gray  
 53 ellipses are their one standard deviations. Solid and dashed arrows indicate the observed and synthetic  
 54 vertical displacement, respectively.  
 55  
 56



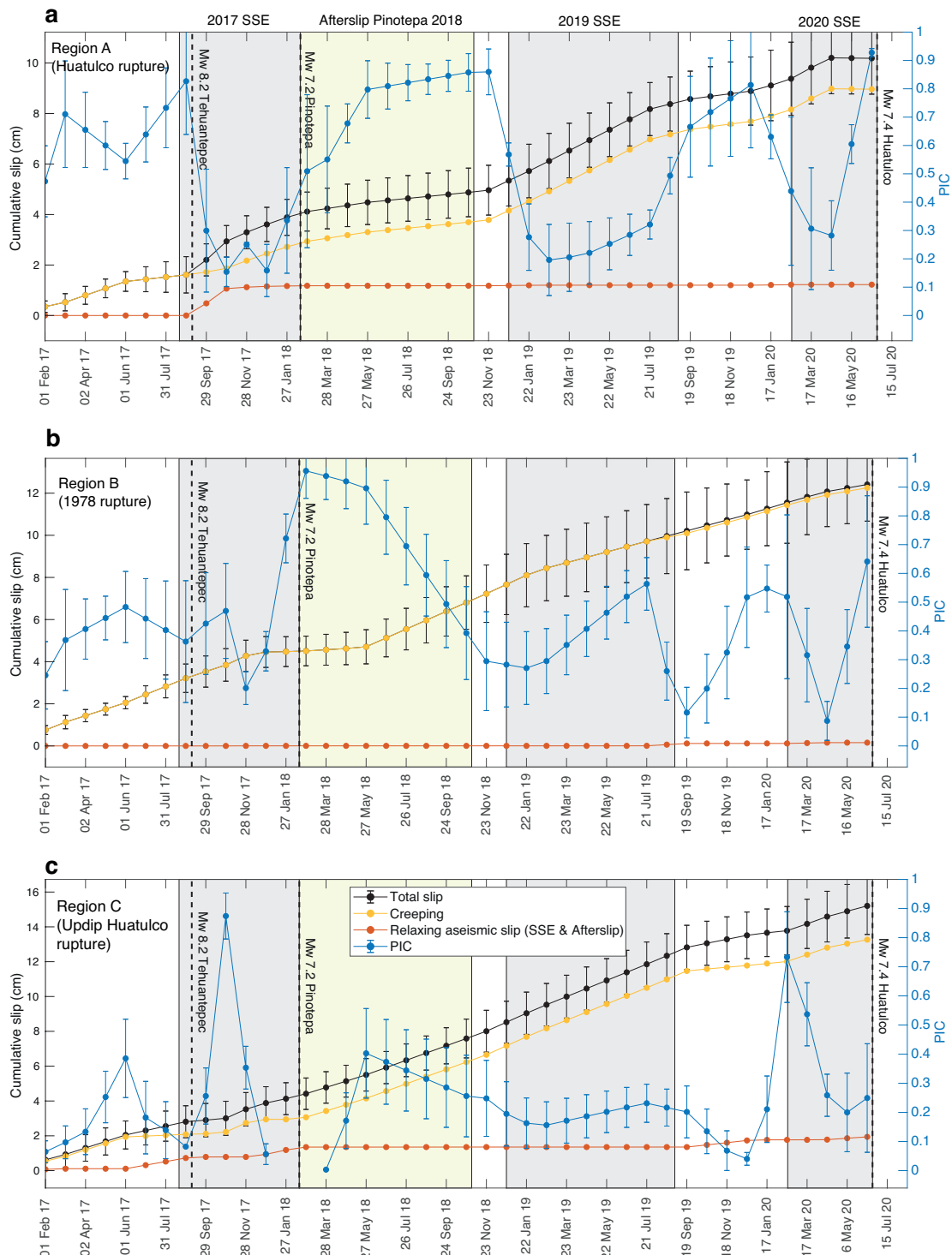
57  
 58 **Fig. 3** GPS inversion of the postseismic deformation of the Huatulco earthquake. **a** North-south displacement  
 59 GPS time series in 4 selected stations. Yellow dots indicate the start and the end of the six 10-day windows  
 60 used for the slip inversions shown in **b**. **b** Aseismic slip inversion for the two months following the Huatulco  
 61 earthquake. Yellow dots represent the aftershocks that occurred during the inversion time-window. Red star  
 62 depicts the hypocenter of the Huatulco earthquake. Slip contours are in centimeters. Thick light gray  
 63 contours are the coseismic slip shown in figure 1a. Dashed regions are the aftershock areas for the 1978 and  
 64 1965 historic interplate earthquakes. Red and blue arrows show the observed and synthetic surface  
 65 displacements, and the gray ellipses one standard deviation of the GPS displacements. Continuous and  
 66 dashed arrows indicate the observed and synthetic vertical displacement, respectively.



81  
 82 **Fig. 4** Evolution of interplate strong interplate coupled regions around the rupture areas of interplate  
 83 earthquakes in Oaxaca. **a** Evolution of regions with PIC > 0.6 before (green patches) and after (warm color  
 84 patches) the 2018 Mw 7.2 Pinotepa earthquake. Red, orange and yellow stars indicate the hypocenter of the  
 85 Huatulco, the 1978 Puerto Escondido and the 2018 Pinotepa earthquakes, respectively. Black contours  
 86 represent the slip isolines of the Huatulco and 1978 Puerto Escondido earthquakes (Mikumo et al., 2002).  
 87 Dashed blue circles represents the areas with radius of 20 km where we analyze the evolution of the interplate  
 88 slip rate and the CFS shown in figures 6, 7c and 7d. **b** Same than **a** but for the 2020 Mw. 7.4 Huatulco  
 89 earthquake. Green line indicates the along-trench profile where the evolution of the aseismic slip and CFS  
 90 on the plate interface is analyzed in Figs. 5,7 and 8.  
 91  
 92



93 **Fig. 5** Evolution of the interplate aseismic slip along the trench within the seismogenic zone of the Oaxaca  
 94 subduction zone. Bottom color scale shows time. Evolution of the **a** total aseismic slip (relaxing aseismic  
 95 slip + creeping), **b** the relaxing aseismic slip (SSEs and afterslip) and **c** the creeping (regions in coupling  
 96 regime) averaged between 10-30 km depth. Hatched regions show the interplate segments with the highest  
 97 moment release of the 2018 Pinotepa, 1978 Puerto Escondido and 2020 Huatulco earthquakes. Stars and  
 98 dashed black lines indicate the along-trench coordinate of the hypocenters. White curves indicate the time  
 99 when the last three long-term SSE began in Oaxaca and the red curve indicates the rupture time of the 2018  
 00 Pinotepa earthquake. Black rectangles enclose the episodes with significant variations of the slip velocity  
 01 (see text). Dashed oblique line in **a** represents the expected total displacement of the incoming Cocos plate  
 02 during the whole period shown by the colorbar.  
 03  
 04



05  
 06 **Fig. 6** Detailed evolution of the aseismic slip in the seismogenic segment of Oaxaca. Evolution of the  
 07 cumulative total slip, creeping, relaxing aseismic slip and plate interface coupling in (a) Region A (the  
 08 Huatulco rupture area), (b) Region B (the 1978 Puerto Escondido rupture area) and for (c) Region C (updip  
 09 region of the Huatulco earthquake). Gray rectangles indicate the occurrence of SSEs in the region. The light-  
 10 yellow rectangle shows the period when the 2018 Pinotepa earthquake afterslip developed in the region.  
 11

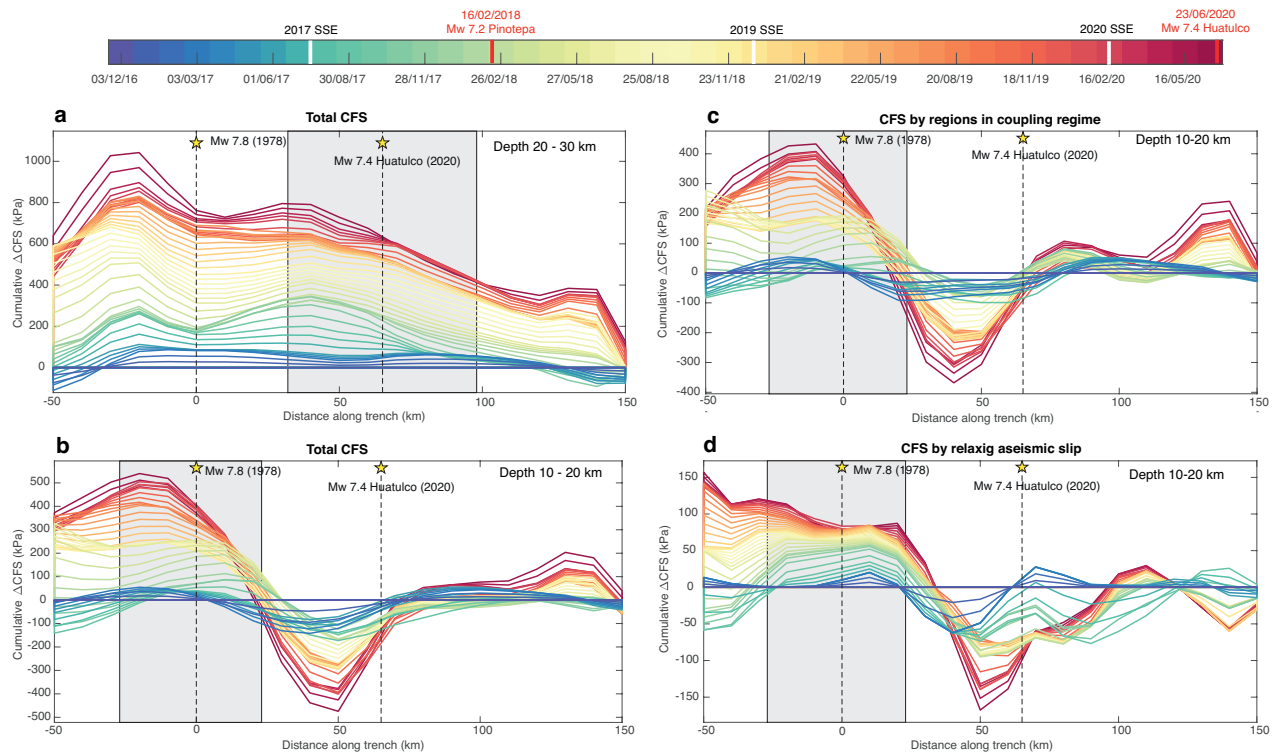


**Fig. 7** Evolution of the CFS in the seismogenic segment of Oaxaca. Evolution of the total CFS along the trench for every 30 days averaged between **a** 20-30 km and **b** 10-20 km depth. Gray rectangles show the interplate segments with the highest moment release of the 2020 Huatulco earthquake and the 1978 Puerto Escondido event (Mikumo et al., 2002). **c** and **d** shows the evolution of the CFS for the band between 10-20 km depth split into the contributions from regions in coupling regime and the relaxing aseismic slip, respectively.

12  
13  
14  
15  
16  
17  
18  
19  
20  
21  
22  
23  
24

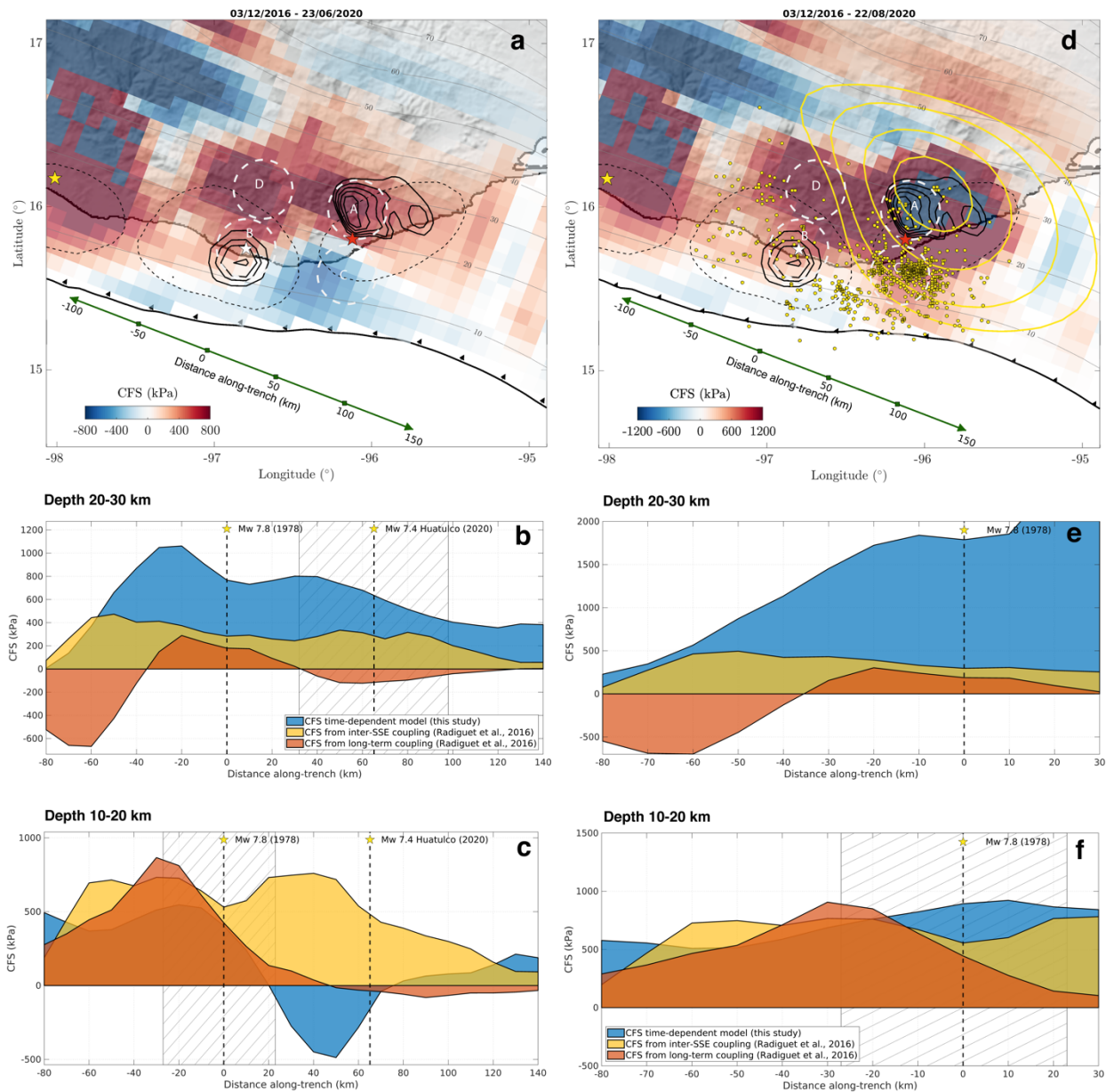
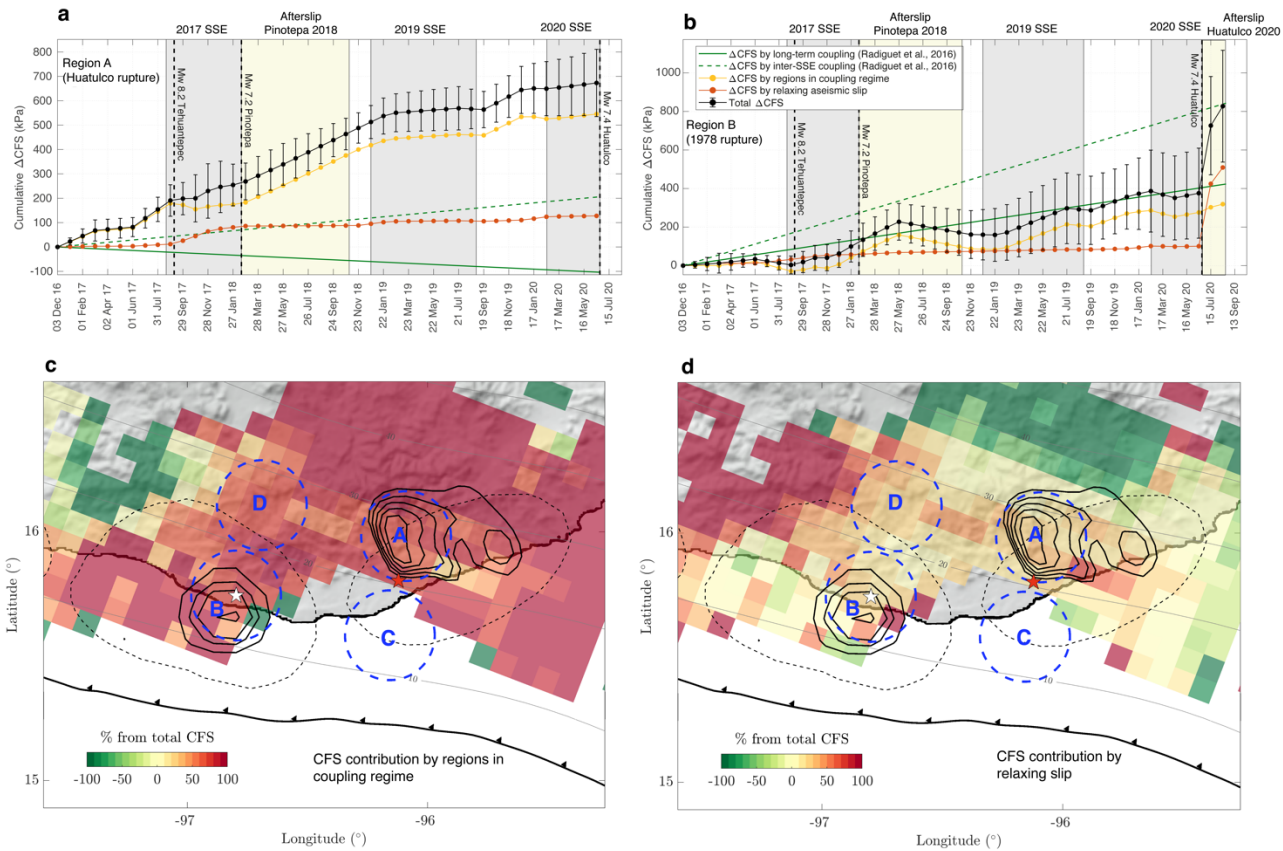


**Fig. 8** Cumulative CFS from the time-variant model and its comparison with the stress built up predicted by time-invariant coupling models. **a** Cumulative CFS in the plate interface between December 2017 and the date of the 2020 Huatulco earthquake. Black contours represent the isoslip values for the 2020 Huatulco and 1978 Puerto Escondido (Mikumo et al., 2002) earthquakes. Black dashed lines delimit the aftershock areas of historic interplate earthquakes. White dashed circles represent the regions where we analyze the evolution of the interplate slip rate and the CFS shown in figures 6, 7c and 7d. **b**, **c** Comparison between our cumulative CFS time-variant model and the CFS predicted by time-invariant coupling models of the region (Radiguet et al., 2016) between December 2017 and the date of the 2020 Huatulco earthquake for two depth bands, between 20-30 km depth and between 10-20 km depth, respectively. **d** Same than **a** but including the stress contributions from the coseismic and postseismic phases of the Huatulco earthquake. Yellow contours are the 5,10,20 and 30 cm slip isolines of the two months cumulative afterslip. Yellow dots depict the 50 days aftershocks after the Huatulco Earthquake reported by the SSN. **e**, **f** Same as **b**, **c** but including the stress contribution from the coseismic and postseismic phases of the Huatulco earthquake focused only in the 1978 rupture segment.



42  
 43  
 44 **Fig. 9** CFS contributions by regions in coupling regime and relaxing slip. **a** and **b** show the evolution of the  
 45 total CFS (black curves) and their contributions from the relaxing aseismic slip (red curve) and coupled  
 46 regions (yellow curve), for the Region A (the Huatulco rupture area) and the Region B (the 1978 Puerto  
 47 Escondido rupture area), respectively. Gray rectangles indicate the occurrence of SSEs in the region. The  
 48 light-yellow rectangle shows the period when the postseismic afterslip of the 2018 Pinotepa and 2020  
 49 Huatulco earthquakes developed in the region. **c** and **d** show the CFS contributions (in %) on the plate  
 50 interface where the total CFS is positive (see figure 8a) by regions in coupling regime and relaxing slip,  
 51 respectively.  
 52

59 Supplementary Materials for:

60  
61 **Slow slip events and megathrust coupling changes reveal the earthquake**  
62 **potential before the 2020 Mw 7.4 Huatulco, Mexico, event**  
63

64 **Authors:** Carlos Villafuerte\*, V. M. Cruz-Atienza, J. Tago<sup>3</sup>, D. Solano-Rojas, R. Garza-Girón, S.  
65 I. Franco, L. A. Dominguez and V. Kostoglodov.  
66

67  
68  
69  
70 \*Correspondence to: villafuerte.cd@gmail.com  
71  
72  
73

74 This document includes:

75  
76 **Methods:**

- 77  
78 1. GNSS time series processing.  
79 2. InSAR images processing.  
80 3. Slip inversion method.  
81 4. Coulomb Failure Stress estimation.  
82

83 **Supplementary Figures S1-S11**  
84  
85  
86  
87  
88  
89  
90

## 91 **Methods**

92

### 93 **1. GNSS time series processing**

94 The GNSS displacement times series are estimated using the GIPSY 6.4 software package (Lagler  
95 et al., 2013), which follows a Precise Point Positioning strategy. The station positions are defined  
96 in the International Terrestrial Reference Frame, year 2014 (ITRF 2014). For daily processing we  
97 used the Jet Propulsion Laboratory final and non-fiducial products (orbits and clocks). We  
98 generated observables using 2 model categories: (1) Earth models and (2) observation models. The  
99 Earth models include tidal effects (i.e. solid tides, ocean loading and tide created by polar motion),  
00 Earth rotation (UT1), polar motion, nutation and precession. Observation models, on the other hand,  
01 are related with phase center offsets, tropospheric effects and timing errors (i.e. relativistic effects).  
02 The troposphere delay is estimated like as random walk process. This effect is broken into wet and  
03 dry components. The azimuthal gradient and the dry component are estimated using GPT2 model  
04 and mapping function (TGIPSY1). The antennas phase center variations are considered through  
05 antenna calibration files. For receiver antennas, the correction is estimated taking the International  
06 GNSS Service (IGS) Antex file. We also applied a wide-lane phase bias to account for the  
07 ambiguity resolution.

08

09 To remove the outliers and then estimate the displacement vectors per time window, we first  
10 determine the data variance for each component and time window from the differences between  
11 daily displacement values and a moving, locally weighted LOESS function (i.e. 2nd order  
12 polynomial regressions with a half-window time support, Figs. 2a, 3a and S6). Then, all data points  
13 in a time window with differences larger than one standard deviation were dismissed. Once the  
14 outliers are removed, a new regression is performed to estimate the final displacement vectors.

### 15 **2. InSAR images processing**

16 We calculate a coseismic interferogram of the Huatulco Earthquake using two single look complex  
17 Synthetic Aperture Radar (SAR) scenes acquired by the Sentinel-1 satellites in the Interferometric  
18 Wide Swath acquisition mode, ascending pass, track 107 (Fig. S2a). The selected scenes were  
19 acquired on June 19<sup>th</sup> and June 25<sup>th</sup>, 2020, which correspond to the pair with the shortest-possible  
20 acquisition span (6 days). The pass and track were selected to provide the best-possible coverage  
21 of the coseismic signal. We use the processing chain provided in the InSAR Scientific Computing  
22 Environment (ISCE) (Rosen et al., 2012) to calculate the interferometric phase between the two  
23 SAR scenes, which includes a coarse coregistration assisted by a digital elevation model (DEM), a  
24 coarse interferogram calculation, a fine coregistration, a fine interferogram calculation, and basic  
25 phase corrections. Accordingly, we additionally use a 1 arc-second DEM from the Shuttle Radar  
26 Topography Mission (Farr et al., 2007) to complete the interferogram formation and topographic  
27 phase correction. Subsequently, we filter the interferometric phase using a Goldstein filter  
28 (Goldstein & Werner, 1998) to later perform phase unwrapping using SNAPHU (Chen & Zebker,  
29 2000). We finally geocode the unwrapped interferogram, convert it to displacement in meters in  
30 line of sight (LOS) geometry and mask out water bodies and areas with spatial coherence lower  
31 than 0.4 (Fig. S2b).

32

33 Geodetic measurements from GNSS and InSAR have different reference frames, which requires  
34 converting one into the other to make a fair comparison of the displacements obtained by each  
35 technique. GNSS measurements are referenced in East, North and Up components, whereas satellite  
36 InSAR have a pixel-wise reference frame in terms of incidence ( $\theta$ ) and azimuth ( $\alpha$ ) angles, which  
37 vary pixel by pixel and define the relative LOS direction towards the SAR satellite. GNSS  
38 displacements can be projected onto the satellite's LOS direction following the expression  
39 (Hanssen, 2001):

40

$$GPS_{LOS} = -\sin\left(\alpha - \frac{3\pi}{2}\right) \sin\theta d_e - \cos\left(\alpha - \frac{3\pi}{2}\right) \sin\theta d_n + \cos\theta d_u$$

where  $GPS_{LOS}$  is the projection of the GNSS displacement vector onto the LOS vector, and  $d_e$ ,  $d_n$  and  $d_u$  are the GNSS displacement components in the East, North and Up directions, respectively. Based on this transformation we adapted the ELADIN inversion method (see next section) so that the Somigliana tensor used to generate the synthetic displacements was projected into the individual LOS unit vectors per InSAR data point to perform the simultaneous GNSS and InSAR data inversion.

### 3. Slip inversion method

The ELADIN (ELastostatic ADjoint INversion) method (Tago et al., 2020) solves a constrained optimization problem based on the adjoint elastostatic equations with Tikhonov regularization terms, a von Karman autocorrelation function and a gradient projection method to guarantee physically-consistent slip restrictions. The method simultaneously determines the distribution of PIC and relaxing slip (i.e. SSEs and afterslip) in the plate interface to explain the surface displacements. Its precision matrix, which corresponds to the inverse of the data variance matrix (see Section 1), allows to minimize the effect of data errors (i.e. cumulative processing errors and non-tectonic physical signals) by weighting the observations. For the pre-seismic and post-seismic GNSS inversions (Figs. 2 and 3), the weights are given directly by the data variance matrix per time window and displacement component (i.e. ellipses around the tips of the horizontal displacement vectors in Figures 2 and 3) (Tago et al., 2020). For the coseismic analysis, where GNSS and InSAR displacements are simultaneously inverted (Figs. 1 and S3c), the data weights were determined by trial and error. The final optimal set of values are such that all InSAR data (i.e. the 221 LOS displacements, Figs. 1b and S2c) were attributed a weight equal to one, while the GNSS data (i.e. 12 displacement components) were weighted according to the epicentral distance of each station as

66 follows. The HUAT and OXUM sites weighed 25, the TNSJ site weighed 15, and the OXPE site  
67 weighed 5, with these values being the same in all three components per site.

68

69 For the coseismic slip inversion, we determined an optimal correlation length of 7 km and a Hurst  
70 exponent of 0.75 for the von Karman inverse-problem regularization function and restricted the slip  
71 component perpendicular to the plate convergence direction to be smaller than 0.6 m (for details  
72 see Tago et al. (2020)). For the pre- and post-seismic slip inversion, we assumed the same Hurst  
73 exponent for the von Karman regularization function, but with correlation length of 40 km to  
74 guarantee high slip restitution in the whole region (Cruz-Atienza et al., 2020; Tago et al., 2020).

75

76 As for the inversion exercise we performed to match the relocated hypocentral depth of 17.2 km,  
77 the results (Fig. S4) significantly improved the data fit (i.e., average errors of  $0.7 \pm 0.6$  cm and  
78  $0.1 \pm 1.4$  cm for GNSS and InSAR data, respectively) and reproduced source characteristics similar  
79 to those of our preferred solution discussed in the main text, which assumes a 3.5 km deeper  
80 interface (Figs. 1a and S3c). However, it is important to point out some differences with that source  
81 model: (1) the maximum slip is significantly larger (4.3 m), (2) the moment magnitude is smaller  
82 ( $M_w$  7.3) as determined from the 1 m slip contour, and (3) the rupture is more concentrated in the  
83 main patch north of the hypocenter, between 18 and 30 km deep. To be consistent with the following  
84 sections (i.e., to use the same interface geometry throughout the manuscript), we keep the deeper  
85 solution shown in Figure 1 for subsequent analysis.

86

#### 87 **4. Coulomb Failure Stress estimation**

88 The total static stress change on the plate interface is the sum of the stress contributions from plate  
89 interface regions that slip, producing either a stress relaxation on the continental crust (SSEs +  
90 coseismic slip + afterslip) or a stress built-up (regions in coupling regime that we modeled as

91 backslip (Savage, 1983)). To estimate the stress tensor, we discretized the 3D plate interface into  
92 triangular subfaults and used the artefact-free triangular dislocation method introduced by Nikkhoo  
93 and Walter (2015) for a half-space. We then compute the Coulomb Failure Stress change ( $\Delta CFS$ )  
94 induced on the plate interface by assuming a locally-consistent thrust mechanism following:

95

96

$$\Delta CFS = \Delta\tau + \mu\Delta\sigma_n$$

97

98 where  $\Delta\tau$  represents the change of the shear stress in the direction of the fault slip (assumed to be  
99 parallel to the plate convergence direction (DeMets et al., 2010);  $\Delta\sigma_n$  is the change of the fault  
00 normal stress (positive for tension); and  $\mu$  is the apparent coefficient of friction assumed to be 0.5.

01

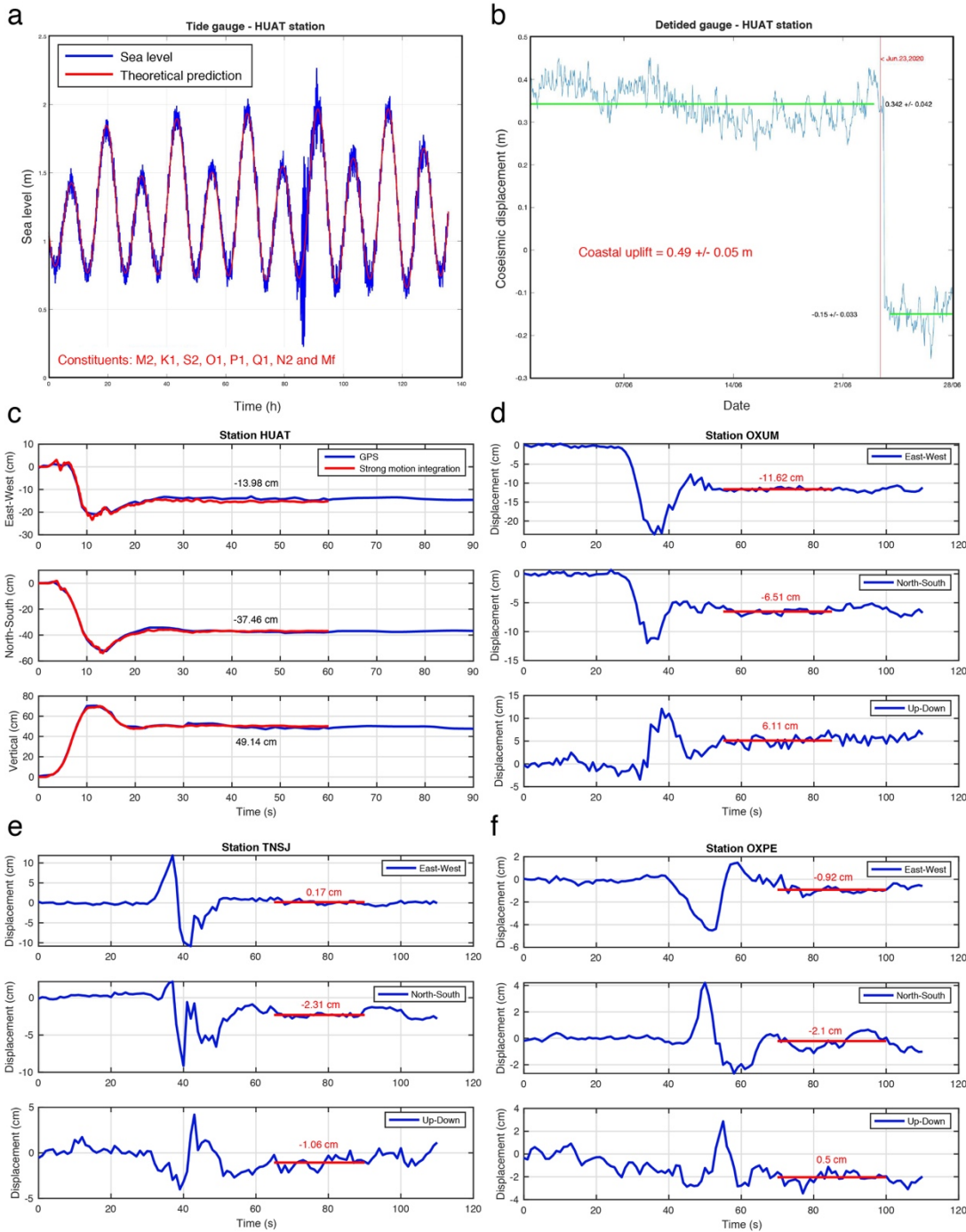
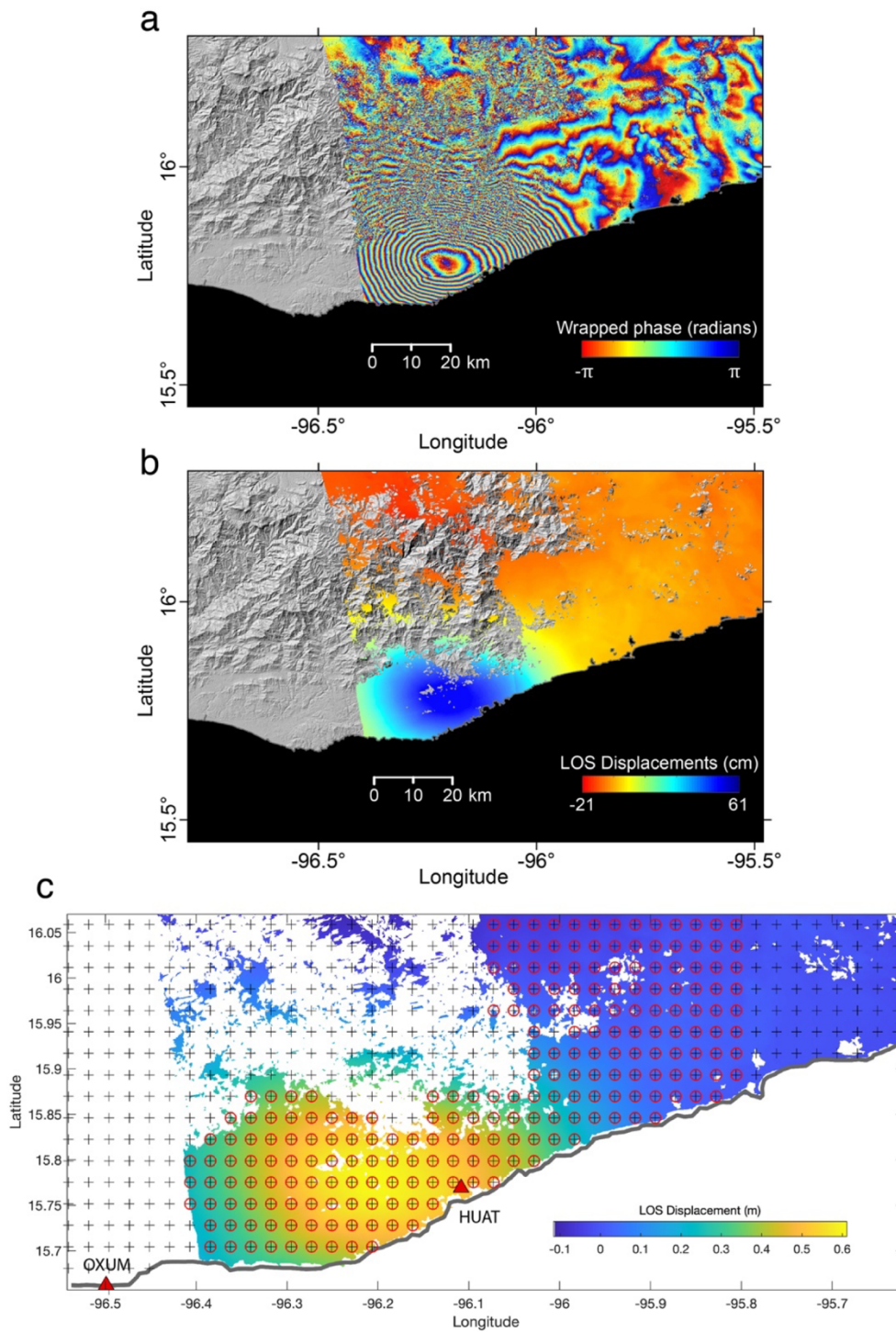
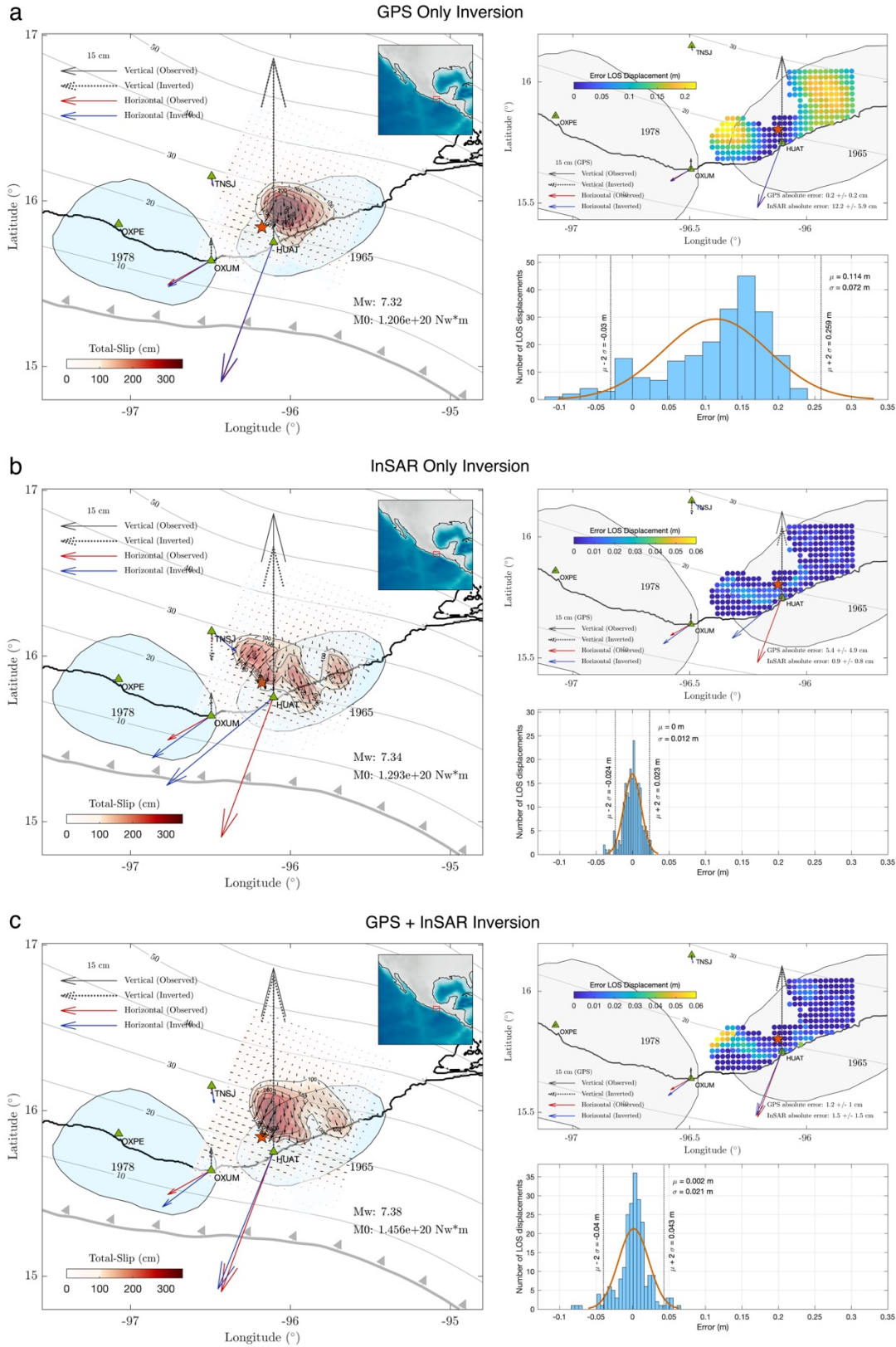


**Fig. S1** Huatulco earthquake co-seismic displacements estimated from the HUAT tide gauge (**a** and **b**); high-rate GPS time series at stations HUAT (**c**), OXUM (**d**), TNSJ (**e**) and OXPE (**f**); and double integration of a strong motion record following the procedure of Wang et al. (2011)(red curve in **c**).

02  
 03  
 04  
 05  
 06  
 07

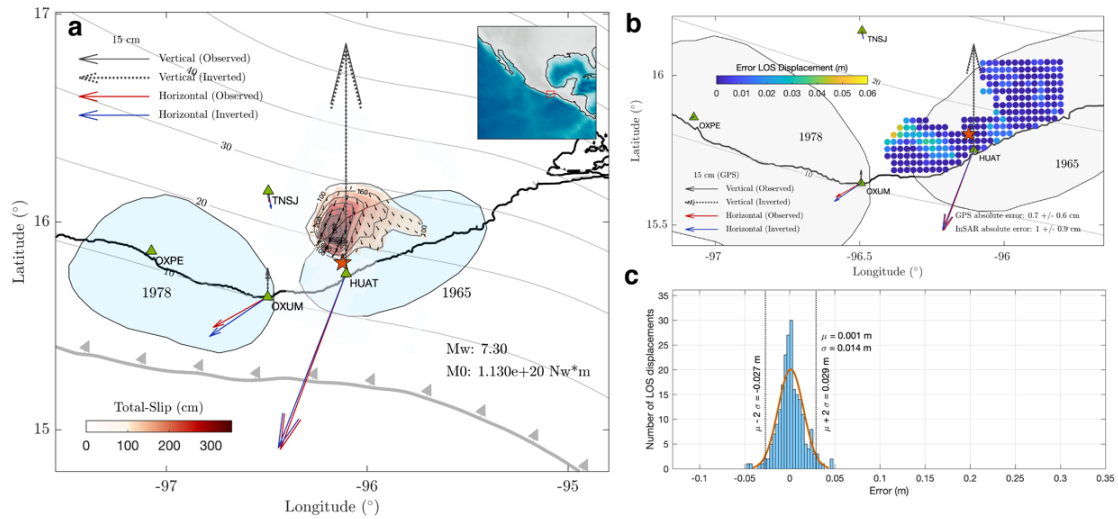


08  
 09 **Fig. S2** Huatulco earthquake InSAR displacements estimated from Sentinel satellite images on Track 107  
 10 Ascending for scenes on June 19 and 25, 2020. **a** Wrapped phase ascending interferogram. **b** Line of sight  
 11 (LOS) displacement from ascending track, positive values correspond to motion towards the satellite. **c** Same  
 12 than **b** but showing the data (circles with crosses) used for the coseismic inversion.  
 13  
 14

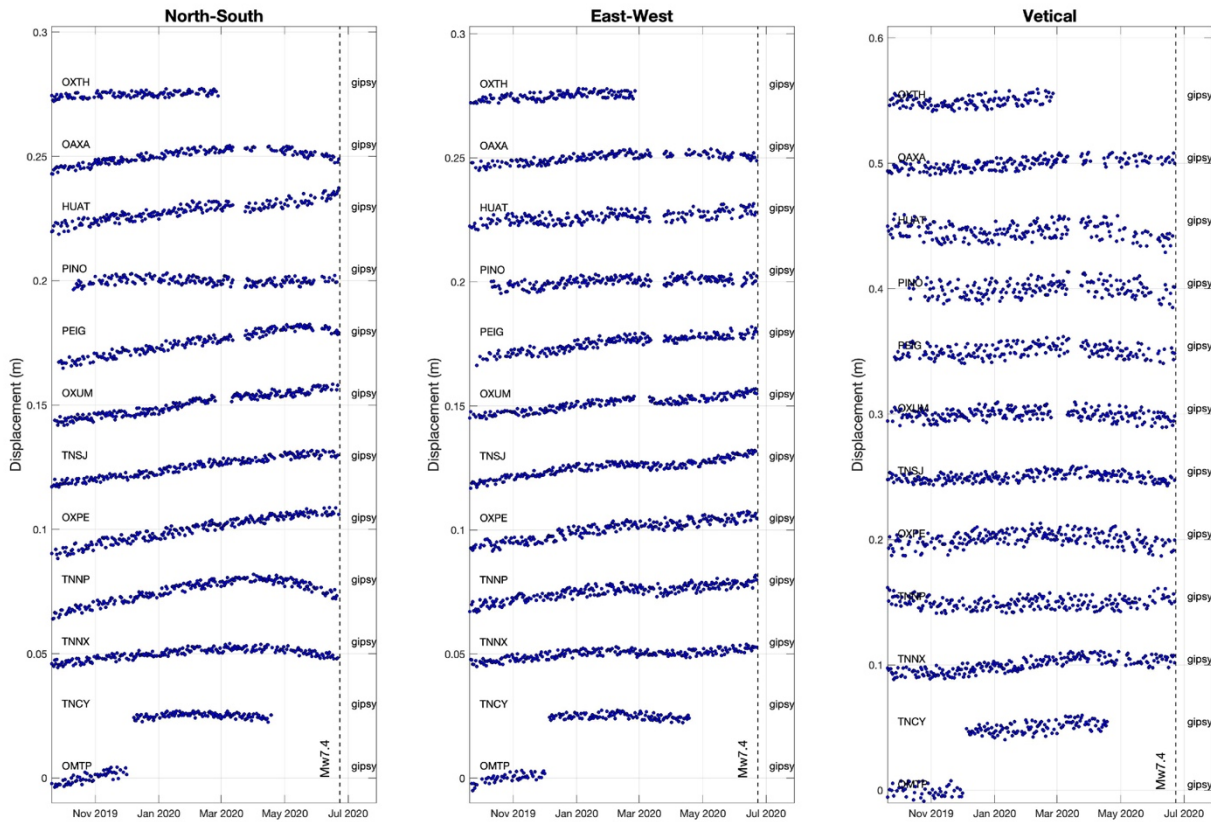


15  
16  
17  
18

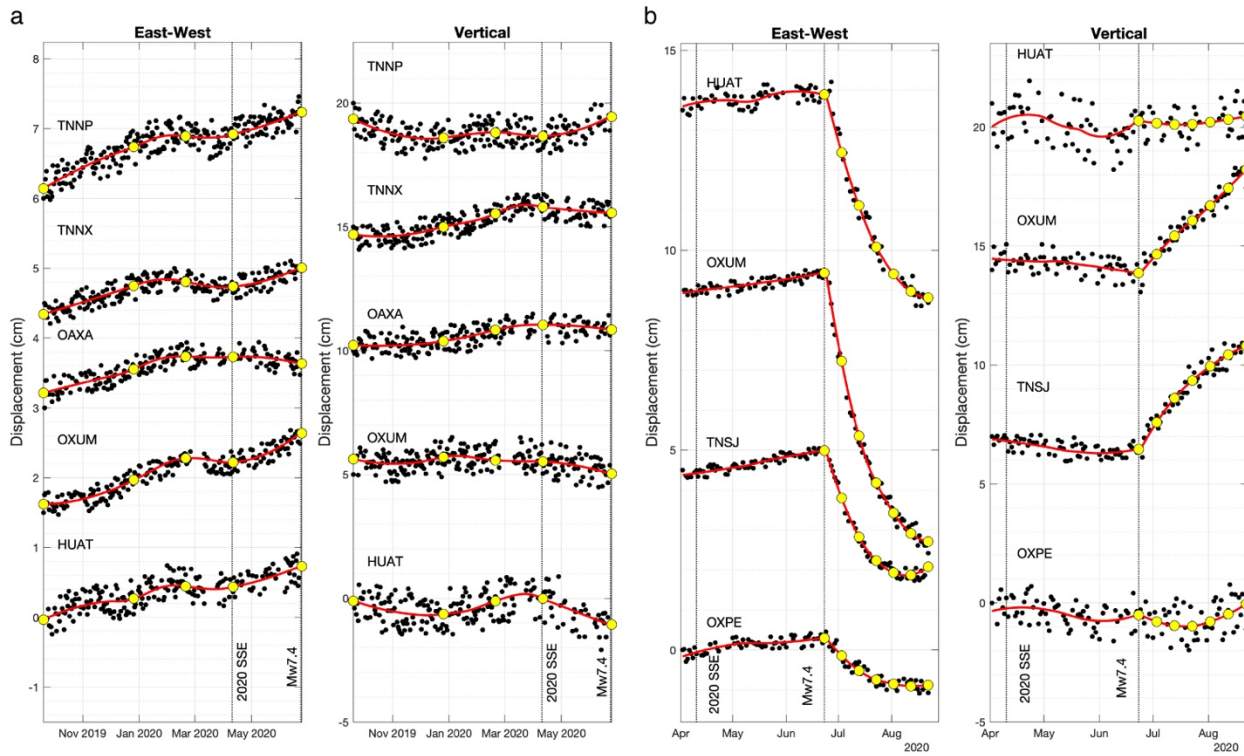
**Fig. S3** Coseismic slip inversions for the Huatulco earthquake using different data sets. Coseismic slip inversion (left panel) and their associated misfit GPS and LOS displacements errors (right panels) using (a) only GPS data, (b) only InSAR data and (c) both GPS and InSAR data.



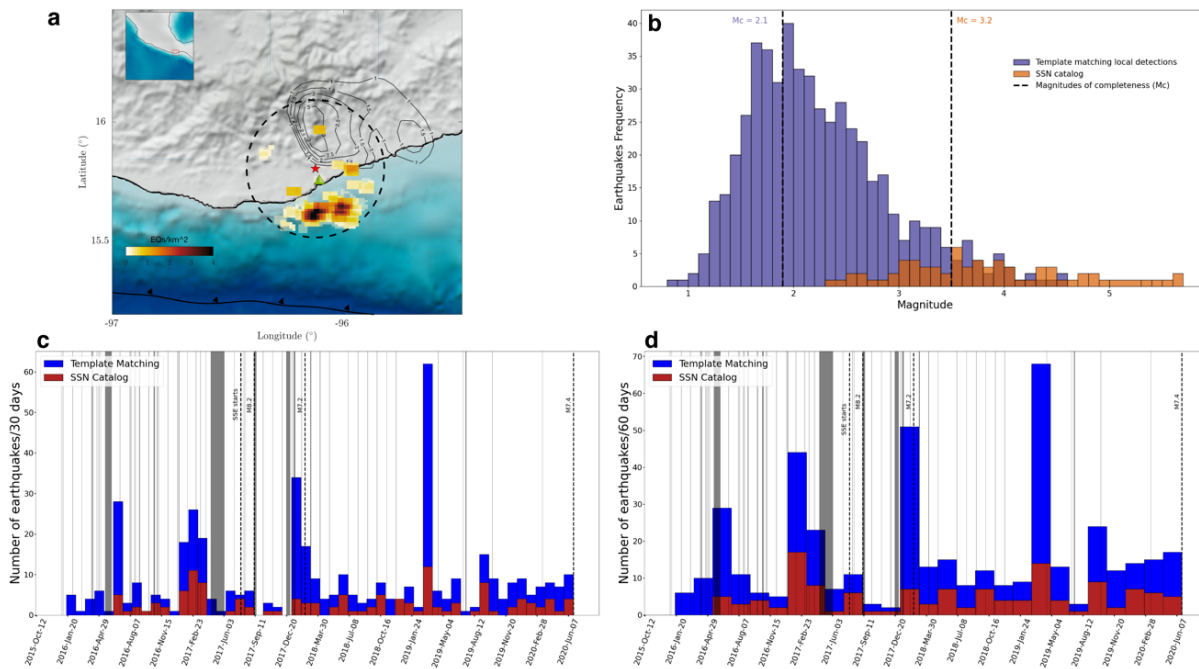
19  
20 **Fig. S4** Huatulco earthquake joint inversion (GNSS and InSAR) assuming that the plate interface has a depth  
21 of 17.2 km at the epicenter (i.e., shifted  $\sim 3.5$  km upwards with respect to the interface shown in Figure S3).  
22 Coseismic slip inversion (a) and their associated misfit GPS and LOS displacements errors (b and c).  
23



24  
25 **Fig. S5** GPS displacement time series estimated with the Gipsy-Oasis (v6.4) software for the pre-seismic  
26 period in the 12 stations and the three components. See Figures 2 and S6.  
27  
28  
29

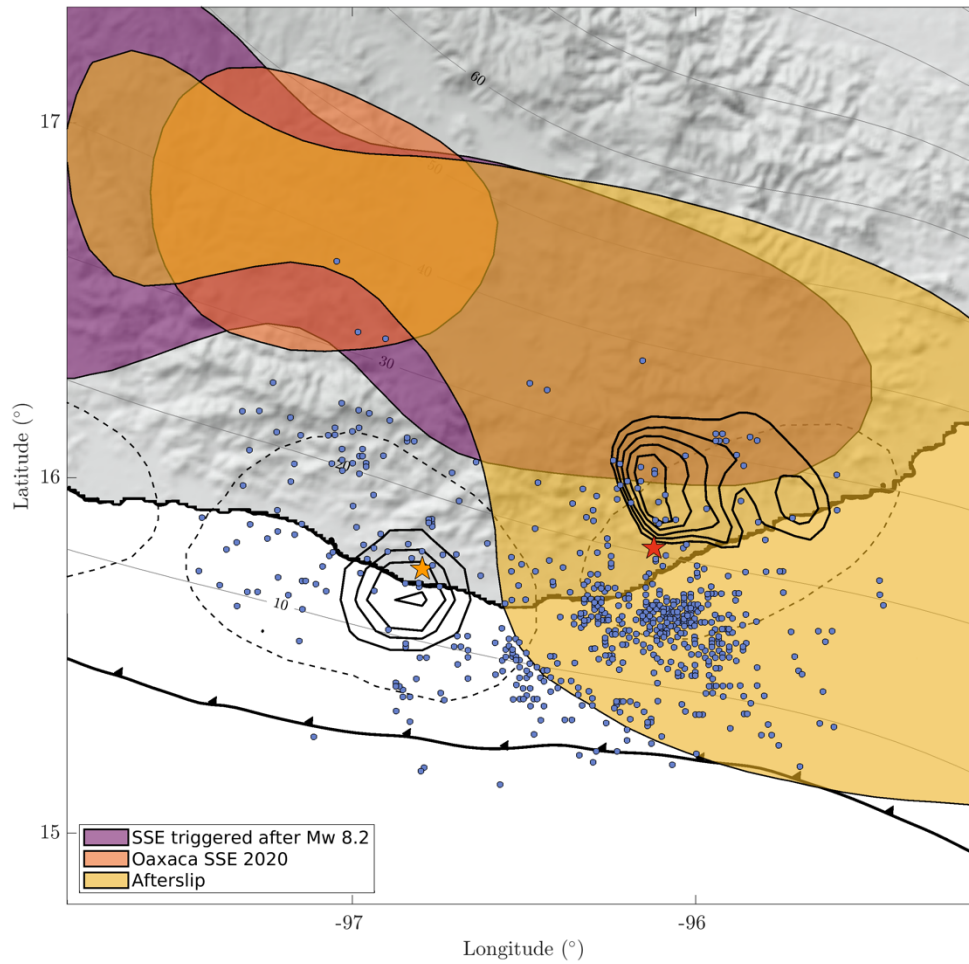


30  
 31 **Fig. S6** East-west and vertical GPS displacement time series estimated with the Gipsy-Oasis software for  
 32 the pre-seismic and post-seismic periods in selected stations shown in figures 2 and 3.  
 33  
 34  
 35  
 36  
 37  
 38  
 39  
 40  
 41  
 42  
 43



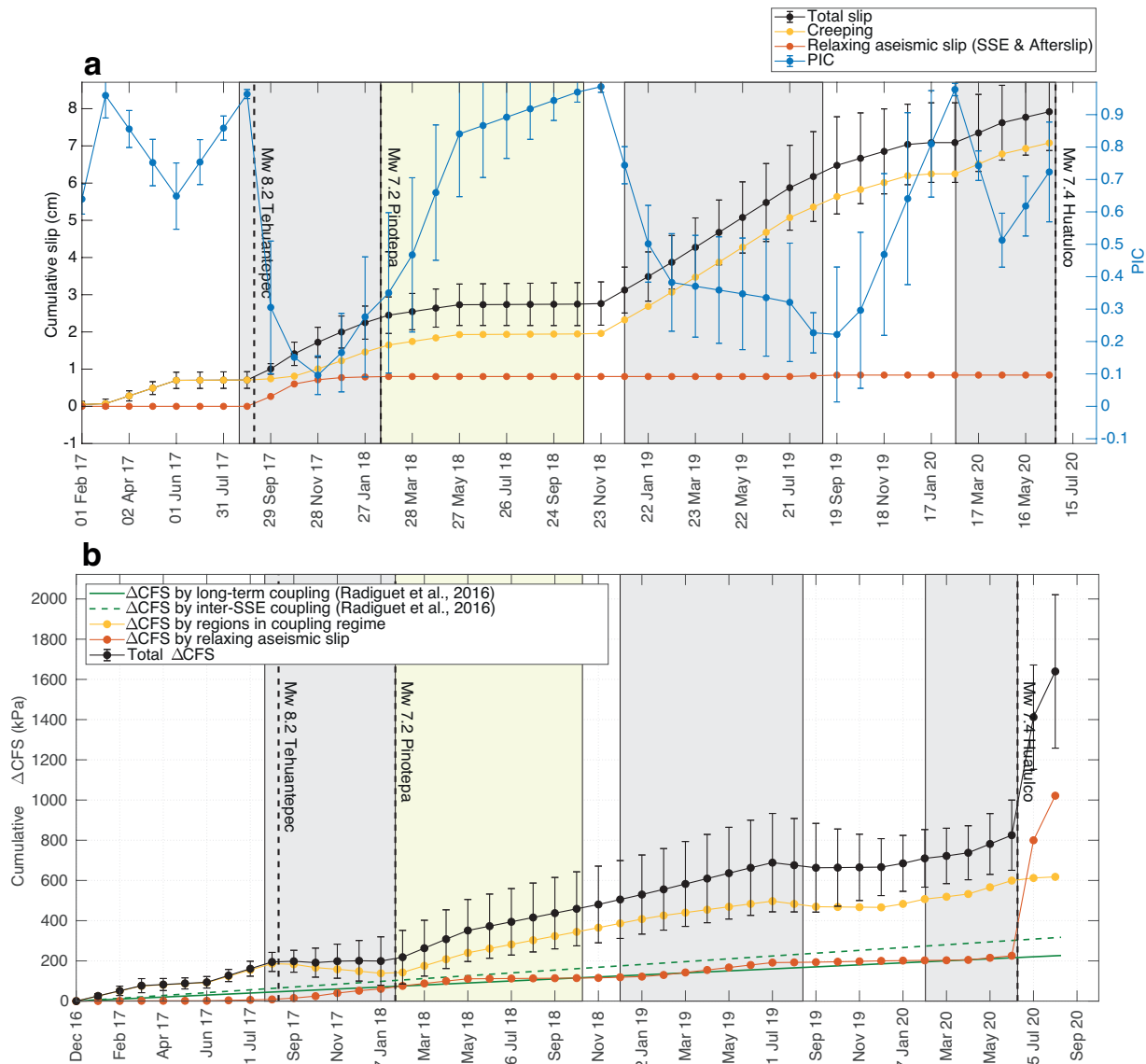
44  
45  
46  
47  
48  
49  
50  
51  
52  
53  
54

**Fig S7** Illustration of template matching (TM) results using the one station method (Cruz-Atienza et al., 2020). **a** Density map of precursor TM detections using the closest station HUIG (green triangle) within 30 km from the Huatulco earthquake hypocenter (red star) and  $M > 2.1$ . Notice how almost all the detections are concentrated updip of the hypocenter due to the scarcity of templates located in the Huatulco rupture area. **b** Frequency distributions for the TM and SSN catalogs and their associated magnitude of completeness. **c,d** Seismicity rate evolution for the TM and SSN for two different earthquake rates. Gray sections indicate data gaps.

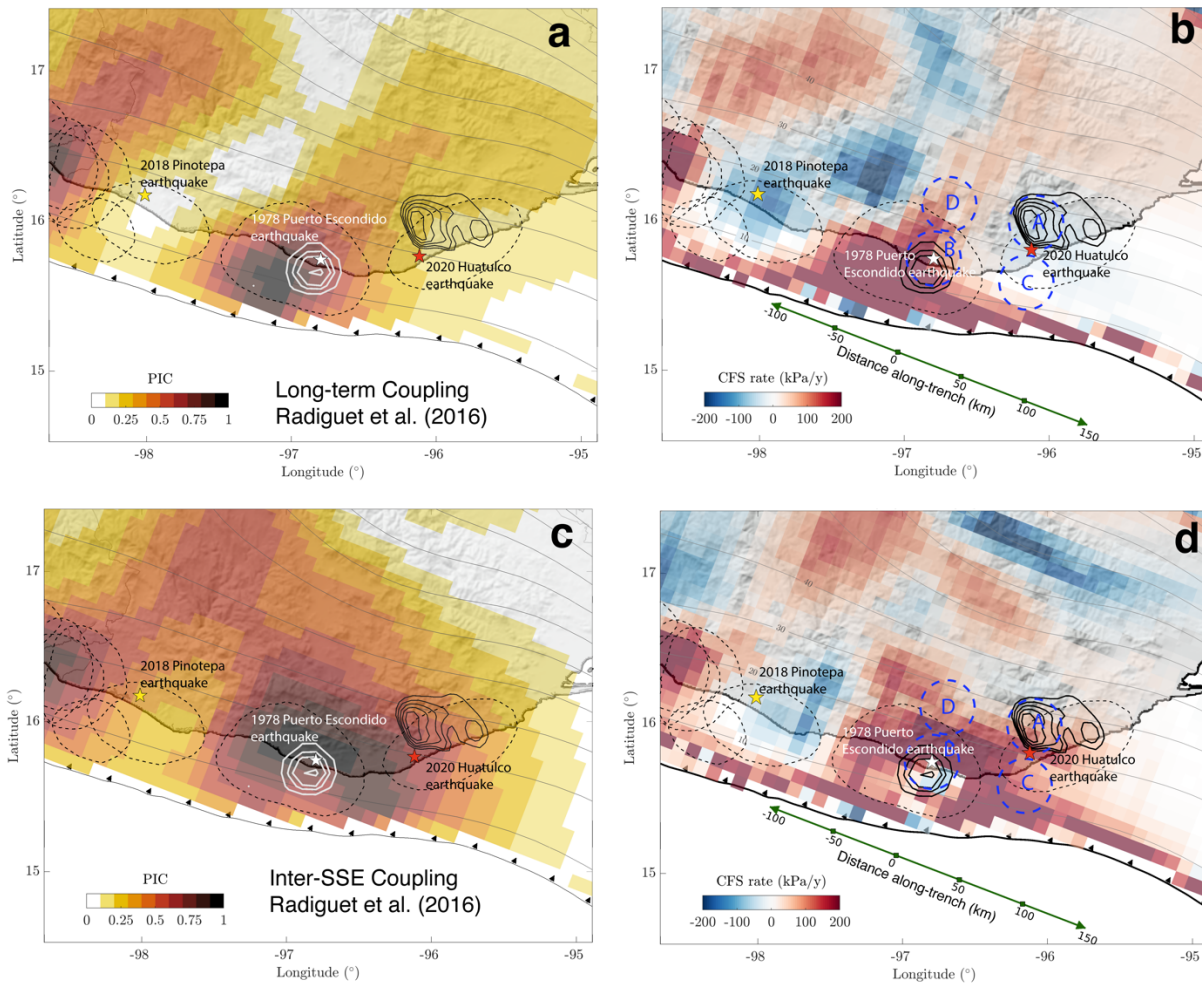


55  
56  
57  
58  
59  
60  
61

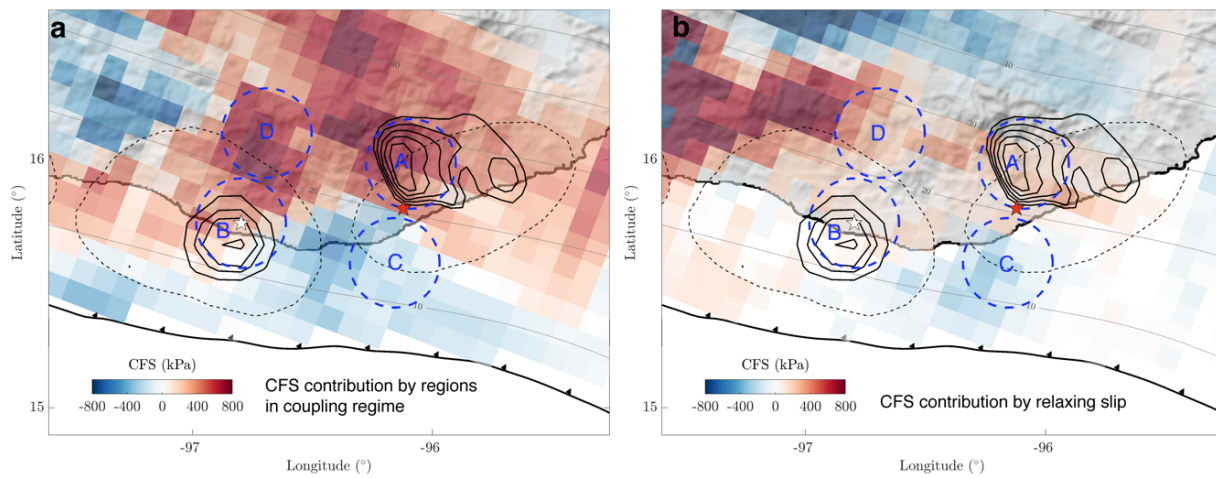
**Fig. S8.** Comparison of the 2017 SSE area (Cruz-Atienza et al., 2020), the coseismic slip distributions of the 2020 Huatulco (red star) and 1978 Puerto Escondido (orange star) earthquakes (black contours), the two months afterslip area following the Huatulco earthquake and the associated aftershock distribution (blue dots).



62  
 63 **Fig. S9** Evolution of different mean quantities in Region D downdip of the 1978 rupture area (Fig. 4). **a**  
 64 Cumulative total slip, creeping, relaxing aseismic slip and plate interface coupling; and **b** the total CFS and  
 65 its components from relaxing slip and coupled interface regions. See Figs. 6 and 9.  
 66  
 67  
 68  
 69



70  
71 **Fig. S10** Long-term and inter-SSE time-invariant interplate coupling models estimated by Radiguet et al.  
72 (2016) for the Oaxaca subduction zone and their associated CFS rates.  
73  
74



75  
76 **Fig. S11** Cumulative CFS contributions in the plate interface between December 2017 and the date of the  
77 2020 Huatulco earthquake associated with regions in coupling regime (a) and relaxing slip (b).  
78  
79  
80  
81

82 **Supplementary References**

- 83
- 84 Chen, C. W., & Zebker, H. A. (2000). Network approaches to two-dimensional phase unwrapping:  
85 intractability and two new algorithms. *JOSA A*, 17(3), 401–414.
- 86 Cruz-Atienza, V.M., Tago, J., Villafuerte, C., Wei, M., Garza-Girón, R., Dominguez, L.A.,  
87 Kostoglodov, V., Nishimura, T., Franco, S., Real, J., 2020. Short-Term Interaction between  
88 Silent and Devastating Earthquakes in Mexico. *Earth and Space Science Open Archive*, 53.
- 89 DeMets, C., Gordon, R.G., Argus, D.F., 2010. Geologically current plate motions. *Geophysical*  
90 *Journal International* 181, 1-80.
- 91 Farr, T. G., Rosen, P. A., Caro, E., Crippen, R., Duren, R., Hensley, S., ... Alsdorf, D. E. (2007).  
92 The shuttle radar topography mission. *Reviews of Geophysics*, 45(2), 1–43.  
93 <https://doi.org/10.1029/2005RG000183>
- 94 Goldstein, R. M., & Werner, C. L. (1998). Radar interferogram filtering for geophysical  
95 applications. *Geophysical Research Letters*, 25(21), 4035–4038.  
96 <https://doi.org/10.1029/1998GL900033>
- 97 Hanssen, R. F. (2001). *Radar interferometry: data interpretation and error analysis* (Vol. 2).  
98 Springer Science & Business Media.
- 99 Lagler, K., Schindelegger, M., Böhm, J., Krásná, H., Nilsson, T., 2013. GPT2: Empirical slant delay  
00 model for radio space geodetic techniques. *Geophys Res Lett* 40, 1069-1073.
- 01 Nikkhoo, M., Walter, T.R., 2015. Triangular dislocation: an analytical, artefact-free solution.  
02 *Geophysical Journal International* 201, 1119-1141.
- 03 Radiguet, M., Perfettini, H., Cotte, N., Gualandi, A., Valette, B., Kostoglodov, V., Lhomme, T.,  
04 Walpersdorf, A., Cabral Cano, E., Campillo, M., 2016. Triggering of the 2014 Mw7.3  
05 Papanoa earthquake by a slow slip event in Guerrero, Mexico. *Nature Geoscience* 9, 829-833.

06 Rosen, P. A., Gurrola, E., Sacco, G. F., & Zebker, H. (2012). The InSAR scientific computing  
07 environment. *Synthetic Aperture Radar, 2012. EUSAR. 9th European Conference On*, 730–  
08 733.

09 Savage, J.C., 1983. A dislocation model of strain accumulation and release at a subduction zone.  
10 *Journal of Geophysical Research: Solid Earth* 88, 4984-4996.

11 Tago, J., Cruz-Atienza, V.M., Villafuerte, C., Nishimura, T., Kostoglodov, V., Real, J., Ito, Y.,  
12 2020. Adjoint Slip Inversion under a Constrained Optimization Framework: Revisiting the  
13 2006 Guerrero Slow Slip Event. *Earth and Space Science Open Archive*, 34.

14 Wang, R., Schurr, B., Milkereit, C., Shao, Z., Jin, M., 2011. An Improved Automatic Scheme for  
15 Empirical Baseline Correction of Digital Strong-Motion Records. *Bulletin of the*  
16 *Seismological Society of America* 101, 2029-2044.

17